

**ANALYSIS OF STEEP DIP SUBSALT SEISMIC ILLUMINATION  
VIA RAY TRACING AND FINITE-DIFFERENCE MODELING:  
A GULF OF MEXICO CASE STUDY**

---

A Thesis Presented to

The Faculty of the Department of  
Earth and Atmospheric Sciences

University of Houston

---

In Partial Fulfillment

of the Requirements for the Degree

Master of Science

---

By:

Annaliese Lee Seyon

August, 2015

**ANALYSIS OF STEEP DIP SUBSALT SEISMIC ILLUMINATION  
VIA RAY TRACING AND FINITE-DIFFERENCE MODELING:  
A GULF OF MEXICO CASE STUDY**

---

Annaliese Lee Seyon

**APPROVED:**

---

Dr. Hua-Wei Zhou, Chairman

---

Dr. Yingcai Zheng

---

Dr. Qingbo Liao

---

Dr. Dan Wells, Dean  
College of Natural Sciences & Mathematics

## **Acknowledgements**

Firstly, I wish to thank my advisor Dr. Hua-Wei Zhou for his positive support and guidance during my research. I also want to thank my thesis committee member, Dr. Yingcai Zheng, for his contributing to the ideas developed in this thesis. I am deeply thankful to my external advisor and manager, Dr. Qingbo Liao, without whose unwavering help and support over the last four years, this thesis would not have been possible. I would like to show my gratitude to all of my colleagues at Repsol who supported me during my research. Especially, I would like to thank Dr. Qunshan Zhang, Dr. German Larrazabal and Fred Shirley for all of their support. I would also like to express my gratitude to Jose Omaña for all of the time he has personally invested in advising and supporting me throughout the pursuit of this degree. I am also deeply grateful to Francisco Ortigosa and Repsol Geophysics management for their support and to Repsol Business Unit and partners for their support and for getting the permission to publish this thesis. My gratitude also goes out to Brigida Fontecha, Dennis Steele and Wenying Cai for their contribution and discussion on this work. I am eternally grateful to Repsol for the sponsorship of my Master's Degree at The University of Houston.

Finally, I would like to thank my mother, Susan Samaroo, whose relentless support and encouragement pushed me to persist in achieving my goals.

*Science proceeds more by what it has learned to ignore than what it takes into account.*

— *Galileo Galilei*

## **Abstract**

This thesis aims to demonstrate the feasibility of improving the seismic depth image of the steeply dipping “attic” regions of the salt feeder of a complex salt body in the deep-water Gulf of Mexico. In order to assess the feasibility of improving the image, the first priority is to determine whether the current data acquired will illuminate the target reservoirs and their trap, given the complexity of the model and the limitations of the acquisition method. My study illustrates and confirms the cause of the previously observed low illumination zone and the possibility of improving the image by incorporating longer offsets or converted waves for imaging.

Firstly, interactive ray tracing and acoustic finite-difference modeling (FDM) are used to assess the low illumination of the steeply dipping salt feeder. Secondly, ray tracing illumination maps and 2D acoustic FDM synthetic images are generated to simulate the impact of full azimuth geometries with source-receiver offsets of up to 8 km and up to 14 km, respectively, in order to determine the benefits of the longer offsets to imaging the subsalt steep dip areas. Thirdly, the contribution of converted waves to imaging the feeder is assessed using elastic FDM and imaging.

The results show that it is impossible to image the steeply dipping portion of the salt root using only P-wave primary reflections, due to the post-critical reflection

of the primary off the steep salt feeder. To see if we can improve the imaging of the steep dip areas by increasing the acquisition offset, the ray tracing result shows no improvement due to limitations of the method, but the more-reliable waveform modeling results show significant improvement in the illumination of steep dips. The improvement is due to the use of prismatic waves in imaging the steep dip attic region of the salt feeder.

Investigation into the contribution of converted waves to imaging the subsalt steep dip areas indicates that elastic imaging has the potential to fill the steep dip illumination holes in the images produced using conventional surface-acquired P-wave data. This modeling study confirms the benefit of acquiring longer offset to improve steep dip subsalt imaging, particularly for using non-primary energy and a sufficiently accurate velocity model.

# Contents

Chapter 1	Introduction .....	1
1.1	Motivation.....	1
1.2	Literature review.....	3
1.2.1	Ray tracing illumination studies.....	3
1.2.2	Ray tracing concepts .....	5
1.2.3	Ray tracing limitations .....	5
1.2.4	Full-wavefield modeling and imaging concepts .....	6
1.2.5	Reverse Time Migration (RTM) .....	7
1.2.6	Ultra-long offset case studies .....	8
1.2.7	Converted wave imaging case studies.....	10
1.3	Goals and Outline .....	12
Chapter 2	Ray tracing illumination analysis.....	14
2.1	Method.....	14
2.1.1	Model building .....	15
2.1.2	Ray tracing parameterization .....	17
2.2	Results.....	19
2.1	Discussion.....	22
2.2	Conclusions.....	27
Chapter 3	2D Acoustic forward modeling and RTM imaging .....	28
3.1	Method.....	28
3.1.1	Acoustic FDM model building.....	30
3.1.2	Acoustic forward modeling parameters .....	32
3.1.3	Imaging of synthetic data .....	34
3.2	Results.....	35

3.2.1	Wavefield snapshot .....	36
3.2.2	Acoustic synthetic seismogram.....	38
3.2.3	RTM Imaging .....	40
3.3	Discussion.....	44
3.3.1	Imaging with prismatic reflections.....	44
3.3.2	Undershooting .....	48
3.3.3	Amplitude and illumination .....	53
3.4	Conclusions.....	55
Chapter 4	Converted-wave forward modeling and imaging.....	57
4.1	Method.....	57
4.1.1	Elastic FDM model building.....	58
4.1.2	Elastic forward modeling parameters.....	60
4.1.3	Imaging of synthetic data .....	62
4.2	Results.....	63
4.2.1	Wavefield snapshots.....	63
4.2.2	Elastic synthetic seismogram .....	66
4.2.3	RTM imaging .....	69
4.3	Discussion.....	71
4.4	Conclusions.....	74
Chapter 5	Summary .....	75

## List of Figures

- Figure 1 A section through the vintage 3D seismic RAZ RTM depth image of the steeply-dipping salt feeder. The encircled area shows the poorly imaged up-dip “attic” regions of the salt feeder..... 2
- Figure 2 A two-layer conceptual model showing shear-wave splitting raypaths of an up-going P-wave at a salt-sediment layer boundary into transmitted P, Pt; transmitted S, St; reflected P, P<sub>r</sub> ; and reflected S, S<sub>r</sub> waves..... 11
- Figure 3 The 3D migration interval velocity model used as input to ray tracing showing a cross section through the complex salt body shown in deep red. Velocity increases from 1500 m/s (blue) to 4500 m/s (deep red)..... 16
- Figure 4 A detailed 3D salt body interpretation showing the complexity of the salt body having: a deep salt layer, salt feeder and rugose canopy. The black dotted lines show the boundaries between each salt feature. The background 3D RTM seismic depth image shows the relatively simple structure of the surrounding sedimentary section. 16
- Figure 5 Subsalt canopy illumination target horizons: shallow (green), intermediate (pink) and deep salt (orange). The background 3D RTM seismic depth image shows a 2D section through the salt canopy. .... 17
- Figure 6 3D illumination hit-count map of the deep salt surface with ray cones shot from the flat-lying subsalt area. Successful rays are shown in green while failed rays are black. The background seismic field data shows a section through the salt canopy. .... 21
- Figure 7 3D illumination hit-count map of the deep salt surface with ray cones shot from the steeply-dipping salt flank toward the west. Black rays are failed rays due to post-critical reflection off of the base of the salt canopy. The background seismic field data shows a section through the salt canopy. .... 21
- Figure 8 Field data RTM section showing the seismic visibility limits of the target horizons. .... 22
- Figure 9 A comparison of seismic RTM image of field data overlain by hit-count for the shallow, intermediate and deep salt horizons using (a) 8 km maximum offset and (b) 14 km maximum offset geometry. The comparison shows increase in hit-count in flat lying areas of the

	targets but little to no increase in the hit-count of the areas up-dip of the reflector visibility limits. ....	23
Figure 10	Common reflection point (CRP) hit-count maps for: (a) 0-8 km offset shallow target (b) 0-14 km offset shallow target (c) 0-8 km offset intermediate target (d) 0-14 km offset intermediate target (e) 0-8 km offset deep salt target and (f) 0-14 km offset deep salt target. Red outline represents the visibility limit interpreted from 0-8 km offset field data with a hit-count of approximately 75 hits. Black outline represents equivalent hit-count limit of 75 hits on the 0-14 km offset maps. ....	24
Figure 11	An enlarged view of the 8 km maximum offset illumination hit-count results encircling short wavelength illumination variations observed in the shallow horizon beneath the rugose base of salt canopy. ....	26
Figure 12	NW-SE 2D line section of the 3D field data RTM drawn through two salt feeders. ....	29
Figure 13	2D velocity model used as input for creating the FDM velocity model. ....	29
Figure 14	Density model built as input to the acoustic variable density FDM algorithm. ....	31
Figure 15	Synthetic seismograms showing (a) the effect of dispersion of the direct waves due to the spatial sampling interval failing to satisfy the dispersion criterion. (b) no dispersion due to the use of an appropriate sampling rate. ....	32
Figure 16	Synthetic wavefield snapshots generated from acoustic FDM. (a-f) show wavefield snapshots 1.2, 1.8, 2.0, 3.0, 4.2 and 4.6 seconds respectively, from a single shot located at location 17 overlaid on the reflectivity model generated from the velocity and density input models. ....	37
Figure 17	Synthetic seismogram computed using acoustic FDM for the same shot location illustrated by the wavefield snapshots in Figure 16. ..	39
Figure 18	RTM raw stack of synthetic data, before the Laplacian filter is applied, showing strong positive amplitude back-scatter noise in white above the shallow salt and along the boundary of the encapsulated mini-basin. ....	41
Figure 19	Source illumination computed from the RTM algorithm. Red color represents high source illumination decreasing to black. ....	42

Figure 20	Laplacian filtered RTM migration stack of 0-8 km offset synthetic data. Encircled area shows no image of the SE flank of the main feeder.....	42
Figure 21	Laplacian filtered RTM migration stack of 0-14 km offset synthetic data. Encircled area shows an increase in coherent amplitudes of the steep SE flank of the main feeder compared to the image of the 0-8 km data. ....	43
Figure 22	Laplacian filtered RTM migration stack of 8-14 km offset synthetic data. Encircled area shows that all of the coherent energy from the steep SE flank of the main feeder is contributed by 8 – 14 km offset data. ....	43
Figure 23	RTM migration stack of 8-14 km offset synthetic data showing the raypath of prismatic waves reflected through the illumination window created by the small-scale concave anomaly (encircled) at the base of salt canopy and off of the steeply dipping salt feeder. ..	45
Figure 24	Source illumination matrix showing illumination windows observed at six locations due to the concave structure of the base of salt. Red color represents high source illumination decreasing to grey. The prismatic raypath reflected off of the SE dipping flank of the main salt feeder is traced in red. Black and green arrows at the surface represent the 8 km and 14 km offset source-receiver spread respectively.....	46
Figure 25	Source illumination matrix showing illumination windows observed at six locations due to the concave structure of the base of salt. Red colors represent high source illumination decreasing to grey. The prismatic raypath traced through the enclosed mini-basin between the two feeders is highlighted. Black and green arrows at the surface represent the 8 km and 14 km offset source-receiver spread respectively.....	47
Figure 26	3D view showing the salt canopy structure (dark purple) and failed (black) and successful rays (light blue) undershooting the canopy from the steep dip flank. The ray cone is shot from the deep salt surface displaying the hit-count through the RTM seismic field data displayed in the background sections.....	50
Figure 27	Map view of hit-count on deep salt surface with failed (black) and successful rays (cyan) undershooting the canopy to the edge of the Sigsbee escarpment (red area).....	50

Figure 28	2D velocity model with deep salt layer replaced with background sediment. ....	51
Figure 29	RTM migration stack of 0-8 km offset synthetic data using the velocity model with salt canopy only.....	52
Figure 30	RTM migration stacks of (a) 0-8 km offset data and (b) 0-14 km offset data migrated using the velocity model with salt canopy only. ....	52
Figure 31	Acoustic impedance section computed from acoustic FDM input velocity and density models. ....	54
Figure 32	A P-wave reflectivity section computed from acoustic impedance volume. Black represents high positive reflectivity and white represents high negative reflectivity. ....	55
Figure 33	2D elastic FDM model including P-wave velocity, S-wave velocity and density attributes.....	58
Figure 34	P-wave velocity model used in acoustic RTM to migrate elastic data and a conceptual ray diagram showing the critical reflection of P-wave ray at the base of salt for an up-going incident ray incident at the critical angle. ....	59
Figure 35	Converted wave model with S-wave salt velocity in the salt layer and a conceptual ray diagram showing the up-going incident P-wave ray and the penetration of the P-S converted ray through the salt. ..	60
Figure 36	Wavefield snapshots generated from elastic FDM. (a-f) show snapshots at 0.0,1.3, 2.1, 2.7,3.2, and 3.9 seconds respectively from a single shot located at with 8 km maximum offset overlaid on the interval layer model consisting of the water layer (blue) supra-salt sediment layer (green), salt-body (red) and the subsalt sediment layer (yellow). ....	65
Figure 37	Synthetic seismogram computed using elastic FDM. ....	67
Figure 38	2D Wavefield snapshots stacked in a 3D cube displaying the wavefield, seismogram and normal incidence raypaths in the three orthogonal planes. ....	68
Figure 39	(a) Synthetic data displayed to illustrate the wavefield snapshot, seismogram and normal incidence/ zero-offset raypath and (b) Interpretation of primary, converted wave and multiple events on the seismogram.....	68

Figure 40	Acoustic RTM of elastic data migrated using the P-wave only velocity model. ....	69
Figure 41	RTM depth migrated section of synthetic elastic data migrated using the converted wave model. ....	71
Figure 42	Comparison of (a) P-wave RTM image and (b) the superimposed P-wave RTM and converted wave image. ....	71

## List of Tables

Table 1	Ray tracing parameterization. ....	18
Table 2	Acoustic variable density input model parameters. ....	31
Table 3	Numerical modeling computation parameters. ....	33
Table 4	2D FDM acquisition geometry parameters. ....	34
Table 5	2D RTM migration parameters. ....	35
Table 6	Elastic finite-difference modeling computation parameters. ....	61
Table 7	Source-receiver geometry of split-spread 8 km maximum offset layout. ....	61
Table 8	Acoustic RTM migration parameters for imaging elastic data. ....	62

# Chapter 1 Introduction

## 1.1 Motivation

Oil and gas companies have downsized their exploration efforts in terms of drilling and seismic acquisition since the steep decline in oil prices during the second half of 2014. As a consequence, increased effort has been placed in innovative technologies and methods for capitalizing on seismic data already acquired in order to improve margins on producing fields and reduce uncertainties in prospecting.

An early vintage rich-azimuth (RAZ) seismic survey was acquired over a producing oilfield in the Gulf of Mexico. The RAZ is the combination of three wide-azimuth (WAZ) surveys with full azimuthal coverage and offsets of up to 8 km. Although a good overall understanding of the study area was developed using advanced 3D TTI RTM imaging of the RAZ data with 360° azimuthal coverage and a detailed well-calibrated velocity model, poorly imaged areas were observed particularly in the up-dip “attic” regions of the structure (Figure 1).

This case study aims to determine the feasibility of improving the seismic depth image of the steeply-dipping “attic” regions of the salt root of a complex salt body in the deep-water Gulf of Mexico since it delineates the limit of the oilfield producing from steeply dipping reservoir beds sealed against the salt.

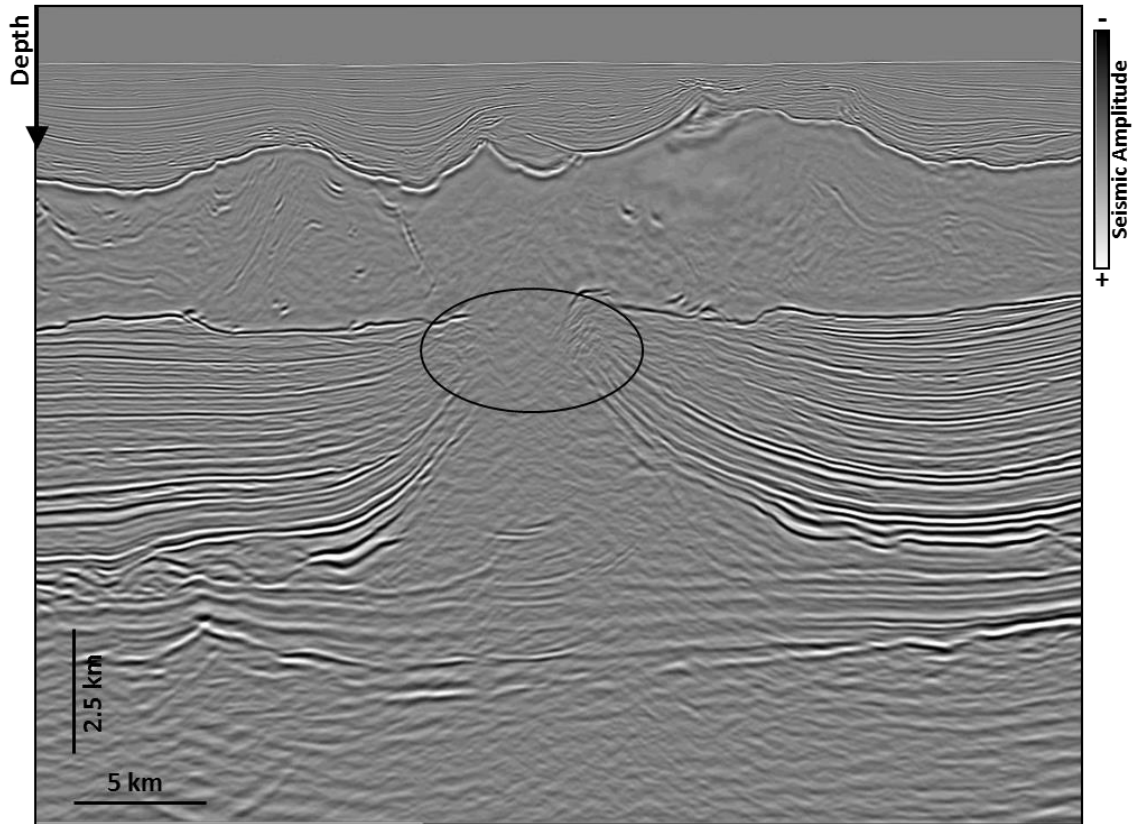


Figure 1 A section through the vintage 3D seismic RAZ RTM depth image of the steeply-dipping salt feeder. The encircled area shows the poorly imaged up-dip “attic” regions of the salt feeder.

In order to understand the feasibility of improving the image, it is first important to determine whether the current data acquired will illuminate the target reservoirs and their trap, given the complexity of the model and the limitations of the acquisition method. The study illustrates the cause of the observed low-illumination zone and investigates the possibility of improving the image by incorporating longer offsets or converted wave imaging.

## 1.2 Literature review

Seismic modeling is very useful to help to explain variations in subsalt amplitude distortions and to optimize the survey design of subsurface targets. One of the most important factors affecting the amplitude of subsurface targets is seismic illumination. Seismic illumination is defined as the migrated amplitude distribution obtainable for a given reflector, velocity field and acquisition geometry in the special case where reflectivity is held constant (Schneider *et al*, 1999). Seismic illumination variations are affected by non-uniform acquisition geometries and lateral velocity variations in the earth. Poor subsalt illumination occurs when the illuminating wavefield suffers amplitude loss due to scattering, absorption, attenuation and mode conversion.

### 1.2.1 Ray tracing illumination studies

Muerdter *et al.*, (1996) used ray modeling to explain the seismic response observed below salt edges. Ray tracing is a fast, flexible and relatively inexpensive method that approximates the one-way downward wavefield propagation. Muerdter *et al.*, (2001) performed a comprehensive ray tracing study to analyze the issues related to complex salt imaging. Their main conclusions were that:

- For flat, tabular salt, ray tracing models the same fold regardless of the thickness but the maximum angle of illumination for a given acquisition geometry is decreased according to the thickness of the salt slab.

- Illumination is affected by the thickness of the salt. Thicker salt reduces the illumination of subsalt reflections.
- The edge of salt typically shows a reduction in the fold.
- The effect of the salt structure extends as much as half of the maximum offset away from the edge.
- The shape of the base of salt affects subsalt illumination more than the top of salt.
- Illumination is greatly reduced when the relative dip of the base of salt approaches the critical angle.
- For dipping slabs, illumination decreases as the relative dip to the target reflector increases. The direction of shooting affects the illumination of targets beneath dipping slabs which affects subsalt AVO response.
- A convex salt shape focuses energy resulting in anomalously high illumination and concave salt shape disperses energy resulting in dim illumination.
- The best illumination occurs when the shooting direction is parallel to the structure.
- Shallow subsalt targets are more affected by salt geometry-related illumination effects than deeper targets.

### **1.2.2 Ray tracing concepts**

Raypaths are conceptual lines that trace the direction along which seismic wavefront propagates. A single raypath describes the propagation of a portion of the entire seismic disturbance pattern from the source, through the subsurface to a single receiver. Raypaths follow three basic rules: they are unbent in a constant-velocity medium; raypath bending occurs at velocity boundaries and bending is governed by Snell's law and Fermat's principle.

For ray tracing, a source location and receiver location are required, in addition to the model containing properties such as P-wave velocity in the simplest case and/or density, S-wave velocity, anisotropic parameters, *etc.* There are several ray tracing modes to consider when conducting a modeling study such as zero offset, common shot and CMP gather ray tracing. 3D CMP ray tracing is a popular method of modeling illumination of the subsurface for 3D acquisition geometries.

### **1.2.3 Ray tracing limitations**

Ray based methods can give poor results in complex areas because the ray theory assumes that interfaces are smooth on a scale length comparable to the wavelength of the P-waves illuminating the target. An asymptotic approximation of the exact solution to the wave equation is computed ignoring the second order terms and higher. Ray tracing is limited to smooth continuous models and can suffer distortions in complex singular regions, (Červený, 2001). Ray tracing methods of

modeling wavefield propagation are also notoriously poor at handling multi-pathing.

However, despite their limitations in describing wave propagation in such complex media and their inability to describe the entire acoustic or elastic wavefield compared with full-wave methods; ray methods still occupy a primary position in many seismic applications because of their relative low cost to acquire, ease of use and speed of computation when compared to full-wavefield modeling techniques. The effect on subsalt amplitudes is more accurately modeled by using full-wavefield modeling methods.

#### **1.2.4 Full-wavefield modeling and imaging concepts**

Finite-difference (FD) modeling followed by two-way full-wavefield migration imaging has become the standard workflow in current seismic numerical full-wavefield forward-modeling methods because of the steadily decreasing cost of computation (Gjøystdal *et al.*, 2002). The finite-difference method transforms a partial differential equation such as the wave equation into a discretized difference equation that can be solved numerically. This is a difference approximation for the derivative of a quantity at one grid point in terms of values at neighboring points.

The finite-difference operator is a frequently used operator (Marfurt, 1984; Carcione *et al.*, 2002; Moczo *et al.*, 2007) and is given by equation (1):

$$\frac{d^2U(x)}{dx^2} = \frac{U(x+dx) - 2U(x) + U(x-dx)}{\Delta x^2} \quad (1)$$

### 1.2.5 Reverse Time Migration (RTM)

Reverse Time Migration (Baysal *et al.*, 1983) is a two-way full-wave equation depth migration algorithm. The first step of RTM is to take the recorded time traces and reverse the order in the time domain. The inverse-time function is used as the source for forward modeling the back propagated receiver wavefield through the model from the receiver locations to the source location. This generates the receiver wavefield,  $R_S$ . The second step in the algorithm is to forward propagate a synthetic source function through the model starting from the true source location, which produces the synthetic source wavefield,  $S_S$ . The classic imaging principle for shot-based migration states that reflectors are located where the forward-propagated source wavefield correlates with the backward-propagated receiver wavefield. The image is constructed by taking the zero-lag correlation of the extrapolated source and receiver wavefields (Claerbout, 1971). At each time step, the source and receiver wavefields are cross-correlated and summed to produce the imaging condition,  $I(z,x)$  such that:

$$I(z, x) = \Sigma_s \Sigma_t S_S(t, z, x) R_S(t, z, x) , \quad (2)$$

where  $z$  and  $x$  represent vertical and horizontal axes respectively, and  $t$  is time (Biondi and Shan, 2002). This produces an image only where the events are coincident in both time and space.

RTM is the only seismic migration method that is able to employ full two-way propagation in the downward continuation process (e.g., Gray *et al.*, 2001; Bednar, 2005). The two-way propagation of seismic waves means consideration of multiple reflections or scatterings. In practice the computation of complicated multiples is feasible only with forward modeling approach, as being implemented in the RTM taking the real shot and receiver positions as the computation “sources”. While most RTM applications used only primary reflections, Youn and Zhou (2001); and Liu *et al.*, (2011) showed the benefit of using multiple reflection in pre-stack depth migration that is possible by the two-way propagating RTM.

RTM can handle wavefields in complex velocity models and steep dips above 70° but suffers from large amplitude backscatter noise that contaminates the image near to sharp velocity contrast interfaces (Diaz *et al.*, 2012). Several methods have been proposed to try to remove this artifact from RTM images (Fletcher *et al.*, 2005; Yoon and Marfurt, 2006; Kaelin and Guitton, 2006; Zhang and Sun 2009).

### **1.2.6 Ultra-long offset case studies**

In addition to improving subsalt illumination, longer-offset data has shown to improve the velocity model building process by helping to better determine more accurate anisotropic parameters and velocity updates from full-wave inversion (Brittan *et al.*, 2013). The benefit of using longer offset data to imaging in complex salt in the Gulf of Mexico has been studied by Li *et al.*, (2010; 2014),

Cogan *et al.*, (2011) and Mandroux *et al.*, (2013) among others. Li *et al.*, (2014) attributed the increase in longer-offset illumination for subsalt events under complex salt structures to the undershooting of the overlying salt complexity.

2D acoustic and elastic FDM and RTM modeling case studies (Li *et al.*, 2010) showed significant improvement in the illumination of subsalt events when comparing maximum offset data of 7 km and 20 km. Cogan *et al.*, (2011) conducted a 3D acoustic modeling case study in the Gulf of Mexico to assess the impact of acquisition offsets on steep dip illumination suggesting that 14 km offsets may illuminate steeply-dipping subsalt targets better than a 7 km offset case. Li *et al.*, (2014) also successfully demonstrated the benefit of ultra-long offsets and further studied the sensitivity of longer offset data to velocity errors which suggested that the undershooting of complex salt bodies is the main benefit to improving subsalt dips.

In this study, ray tracing illumination was used to assess the possible imaging impact of newly available longer offset full-azimuth (FAZ) data on steeply dipping reservoir beds near the salt feeder. However, since in complex geology ray tracing may fail to adequately model wave propagation, full-wavefield modeling using FDM was also done to validate the ray tracing results.

### 1.2.7 Converted wave imaging case studies

As a seismic wave propagates through the earth, and through a high velocity layer such as salt, the waves will be subject to energy partitioning at the salt-sediment interfaces into transmitted and reflected shear waves and post-critically reflected P-waves. The proportion of total energy that is reflected as P-P waves increases with an increase in P-wave velocity contrast at the boundary leaving less energy to penetrate through the salt. This also decreases the P-wave critical of incident waves at non-zero incidence angle. Shallow salt layers have the tendency to reduce the net energy available for illuminating subsalt events using P-waves only. Consider an up-going P-wave reflection from a subsalt target incident at the base of salt (Figure 2). The energy of the incident wave is split into transmitted and reflected P and S-waves. This can be similarly represented for the down-going P-wave as well as the up-going and down-going S-wave. The energy partitioning at the interface is given by the scattering matrix (Aki and Richards, 1980) in terms of P-wave velocity; S-wave velocity and density. At low angles, P-P reflection is more efficient than P-S conversion however, at incident angles beyond the critical angle, converted wave paths are more efficiently transmitted through the salt.

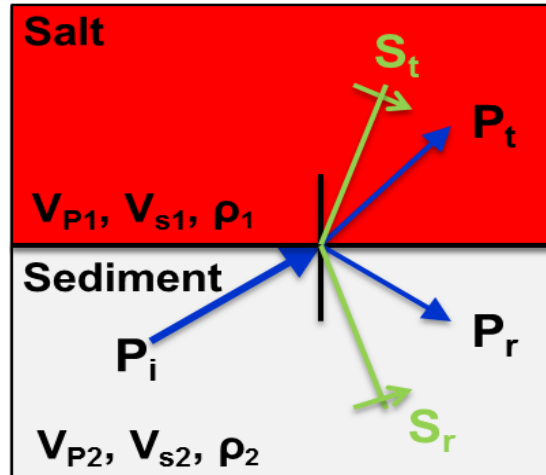


Figure 2 A two-layer conceptual model showing shear-wave splitting raypaths of an up-going P-wave at a salt-sediment layer boundary into transmitted P,  $P_t$ ; transmitted S,  $S_t$ ; reflected P,  $P_r$ ; and reflected S,  $S_r$  waves.

The application of converted waves in imaging beneath high velocity layers such as salt canopies has proven to be beneficial in several studies. Purnell, (1992) showed through physical modeling an increase in dips imaged below a high velocity layer (HVL) by using raypaths that had at least one P-S mode conversion at the base of the HVL. Ogilvie and Purnell, (1996) used elastic forward modeling followed by one-way selective wave-equation migration method of migrating of PSPP and PPSP converted wave modes to illustrate the impact of converted waves on the imaging of subsalt events. The converted wave energy was shown to be quite substantial and if properly exploited can contribute to the image of subsalt reflections compared to with acoustic imaging. Wu *et al.*, (2010) investigated the survey efficiency of different converted wave paths through reflectivity evaluation and demonstrated the improvement of pre-stack converted-path imaging on steep

dip illumination using a simple salt layer. This was done by computing elastic synthetic data and migrating using a hybrid reflection-transmission Born method.

### **1.3 Goals and Outline**

The first objective of this thesis is to model illumination of the understand the low illumination of the steeply dipping salt feeder through forward modeling using interactive ray tracing and acoustic finite-difference modeling (FDM).

The second objective is to simulate the impact of full-azimuth geometries of up to 8 km and up to 14 km respectively, in order to determine the contribution of the longer offsets to the steep dip image. This is done using ray tracing illumination and 2D acoustic FDM methods.

The third objective is to assess the potential contribution of converted waves to increasing the dip range of the illuminated subsalt image. This is done using 2D elastic FDM and comparing RTM migrated images using a P-wave only model and the same model replacing the salt velocity with S-wave salt velocity to image the converted waves at the salt boundaries.

Chapter 2 describes in detail the ray tracing illumination analysis done in order to illustrate the cause of the poor signal-to-noise ratio, and to assess the impact of longer offset data on the illumination of steep subsalt dips. First I describe the input data used in this study, followed by the method and results of using

interactive ray tracing to understand the raypaths from the surface to the steeply dipping target. This is followed by the method and results of target-based modeling of the illumination of two different offset geometries. This chapter also describes the results, discussion and conclusions of this experiment.

Chapter 3 describes in detail the acoustic full-wavefield modeling and imaging analysis used to assess the contribution of longer offset data to the imaging of steep subsalt dips. First I describe the model building process followed by the parameterization of the forward modeling algorithm used, and subsequent imaging. Then the results of the comparison of the two different offset geometries are compared and discussed.

Chapter 4 describes the elastic full-wavefield modeling and imaging method used to assess the impact of converted wave illumination using a simple model. First I describe how the model is built, followed by the parameterization of the elastic FDM algorithm and results of the image comparing the acoustic imaging with converted wave imaging.

Chapter 5 summarizes the conclusions of each experiment, caveats of the study and suggestions for future work in analyzing the problem of steep dip subsalt illumination.

## **Chapter 2 Ray tracing illumination analysis**

Ray tracing analysis is a fast, convenient method of modeling wavefield propagation. Ray-based illumination analysis is typically conducted by tracing raypaths through a velocity model in order to determine whether a given acquisition setup will record the wavefield as it travels into the subsurface and is reflected and scattered. The objectives of this chapter are to illustrate the raypaths reflected from the steeply dipping flank of the salt in order to understand the reasons for the poor signal-to-noise in that area of the image and to determine the impact of increased acquisition offset on illumination of the subsalt targets. The purpose of modeling the illumination of the subsurface horizons is to predict what subsurface features may be imaged by the given acquisition geometry. By modeling the illumination of the surface for different source-receiver geometries, some inferences can be made about the potential impact on the quality of seismic data acquired with different acquisition layouts.

### **2.1 Method**

This section describes the models and workflow used in conducting the ray tracing illumination analysis in this study area located in the Gulf of Mexico. This workflow requires an input velocity model and subsurface horizon interpretation as well as the surface source-receiver geometry used to acquire the field data. First

I describe the input model used in ray tracing followed by a description of the parameterization of the ray tracing and results of the method.

### **2.1.1 Model building**

This target-based illumination analysis method requires three inputs: The gridded velocity model, surface source-receiver geometry and the subsurface target horizons intended to be illuminated by the defined acquisition layout.

The velocity model (Figure 3) used in this target-based ray tracing analysis was obtained from the 3D RTM migration velocity model of the marine vintage RTM depth migration of the field data in the study area (Figure 1). The model features a smoothly laterally varying background velocity trend and a complex two tiered salt body with an extensive salt canopy of an average of 2km thickness and a deep salt layer at an average depth of 11 km (Figure 4). The velocity model was previously built using TTI tomographic migration velocity inversion during an extensive pre-stack depth migration model building process.

Three target horizons (Figure 5) were used in this analysis with the objective of determining the limits of illumination on events of different depths from the base of salt and dip ranges. These were: a shallow reservoir target layer, intermediate reservoir target layer and deep salt layer.

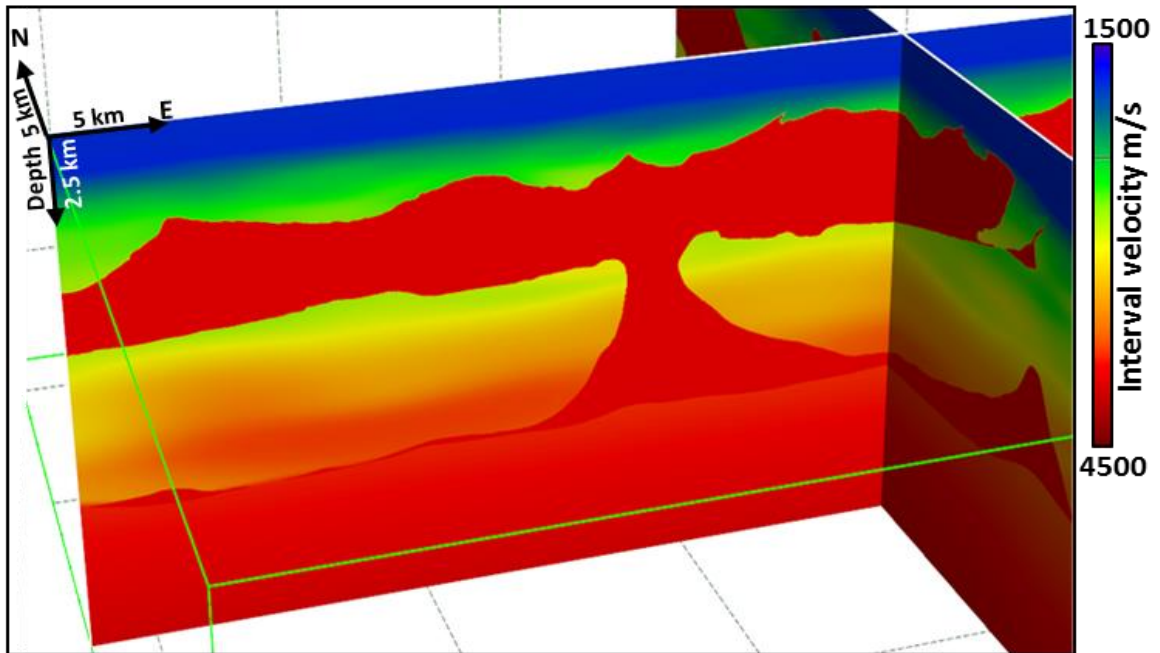


Figure 3 The 3D migration interval velocity model used as input to ray tracing showing a cross section through the complex salt body shown in deep red. Velocity increases from 1500 m/s (blue) to 4500 m/s (deep red).

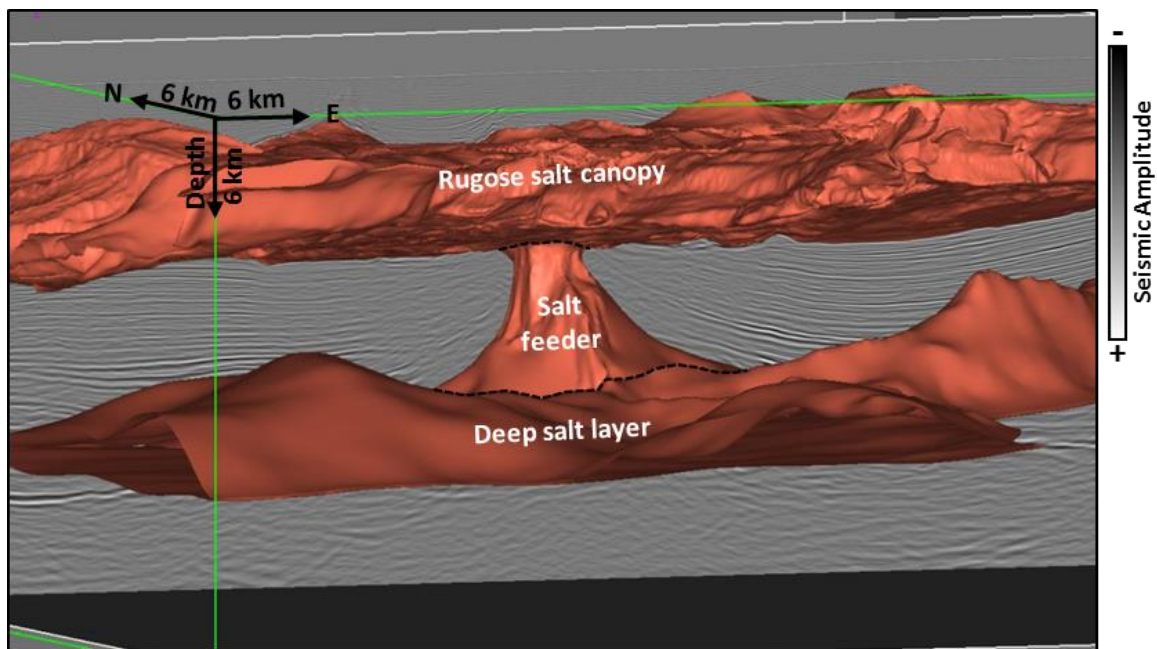


Figure 4 A detailed 3D salt body interpretation showing the complexity of the salt body having: a deep salt layer, salt feeder and rugose canopy. The black dotted lines show the boundaries between each salt feature. The background 3D RTM seismic depth image shows the relatively simple structure of the surrounding sedimentary section.

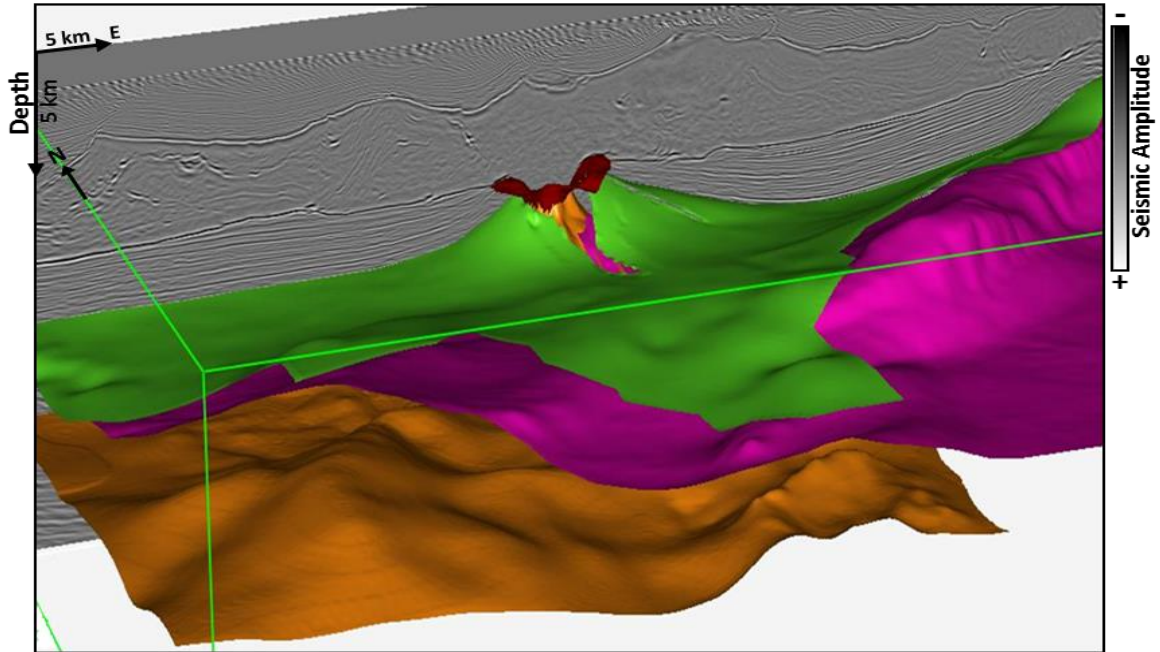


Figure 5 Subsalt canopy illumination target horizons: shallow (green), intermediate (pink) and deep salt (orange). The background 3D RTM seismic depth image shows a 2D section through the salt canopy.

### 2.1.2 Ray tracing parameterization

Ray tracing illumination maps were computed using Paradigm Epos3 ray tracing shooting application. This program uses a 3D common reflection point (CRP) ray cone shooting method from the subsurface targets to surface geometry layout to simulate ray coverage of a subsurface reflection point. In order to model the illumination for the acquisition geometry of the marine field data, the CRP ray cone was parameterized to represent the  $0^{\circ}$  to  $360^{\circ}$  azimuth range of the RAZ acquisition geometry and source-receiver offset range from 0 to 8 km. In practice, the ray cone parameterization was optimized by shooting interactive ray cones starting with a maximum opening angle of  $36^{\circ}$ . These parameters were optimized

to maximize illumination in the relatively flat subsalt areas relative to the base of salt where illumination is expected to be the highest. Table 1 shows the 3D CRP ray tracing parameters used to compute the illumination maps.

<b>3D CRP Ray Cone Parameters</b>	
Input data	Isotropic velocity model, Target surfaces
Maximum subsurface angle	36°
Subsurface angle sampling	1 °
Azimuthal range	0-360 °
Raypath sampling	10 m
Maximum Offset	8 km

Table 1 Ray tracing parameterization.

Illumination hit-count is measured by the proportion of rays that are successfully acquired within the acquisition layout at the surface relative to the total number of rays. Modeled source-receiver ray pairs are flagged as successful if they satisfy the following criteria:

- They can be traced through the model space from source locations to target and back to the surface within the model boundaries. Ray pairs with at least one path that hit the model boundary are eliminated causing an illumination edge effect. The model must therefore be sufficiently extensive to avoid these effects in our target area.

- They fall within the defined aperture. The ray pairs that fail to complete their path from the surface to the reflection point and back to the surface within the defined aperture are eliminated.
- They fall within the acquisition geometry grid defined at the surface, *i.e.*, they satisfy minimum and maximum offset criteria and also source-receiver azimuth criteria. This is particularly important for narrow azimuth (NAZ) surveys as this limited aperture on the cross-line direction tends to reduce the overall illumination hit-count. However since the survey has full azimuthal coverage, the offset and aperture are the more critical criteria than azimuth to consider in this case. Rays that fail to satisfy the geometry criteria are not eliminated, but they are flagged as failed in order to compare the different geometries.

## **2.2 Results**

Target-based illumination hit-count maps are generated by shooting a nominal number of rays at regular interval over a subsurface target. The hit-count is the number of successful rays out of the total number of rays shot per bin. Figure 6 shows a 3D oblique view of a set of ray cones traced through the 3D RTM seismic volume from a relatively flat area on the deep salt target surface. The ray cone shows successful ray pairs in green and the failed rays in black. The colors on the surface represent the hit-count of successful rays. High illumination is shown in

red while low illumination is shown in purple. These results show that there is good illumination where the target surface has a low dipping angle compared to the overlying base of salt and illumination decreases with increasing dip angle of the subsurface target. The very-high illumination in red toward the south is due to undershooting of the canopy at the edge of the Sigsbee escarpment.

Interactive 3D CRP cones were shot from the steeply dipping salt flank producing a ray cone with only failed rays that reflect from the surface to the flank and back into the subsalt section (Figure 7). The purple area on the target shows no illumination, which is attributed to the post critical angle reflection of the rays from that area. Figure 7 shows multiple post-critical reflections along the base of salt which explains why the energy was not recorded at the surface. The CRP hit-count maps of RAZ acquisition geometry with 14 km and 8 km maximum offsets were computed for each of three subsurface targets.

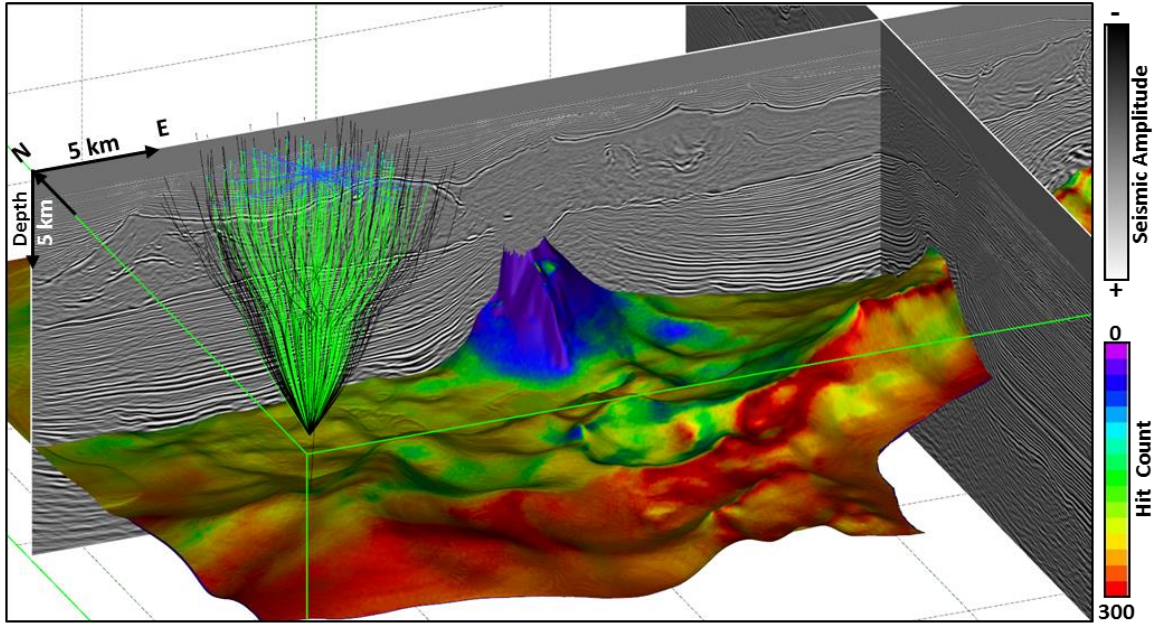


Figure 6 3D illumination hit-count map of the deep salt surface with ray cones shot from the flat-lying subsalt area. Successful rays are shown in green while failed rays are black. The background seismic field data shows a section through the salt canopy.

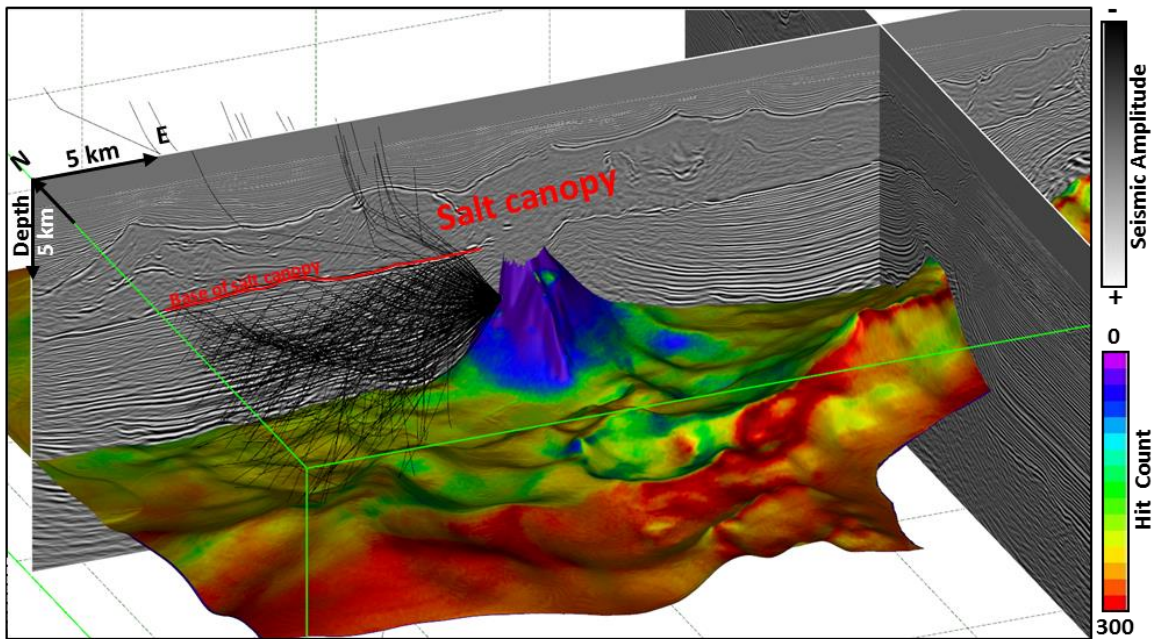


Figure 7 3D illumination hit-count map of the deep salt surface with ray cones shot from the steeply-dipping salt flank toward the west. Black rays are failed rays due to post-critical reflection off of the base of the salt canopy. The background seismic field data shows a section through the salt canopy.

## 2.1 Discussion

In order to relate the illumination hit-count to the field seismic data, visibility limits (Figure 8) were identified in the seismic section as the up-dip limit of event interpretability for each target horizon and provides an interpretive reference. These limits were correlated with the illumination hit-count maps for the 8 km maximum offset illumination hit-count maps (Figure 9).

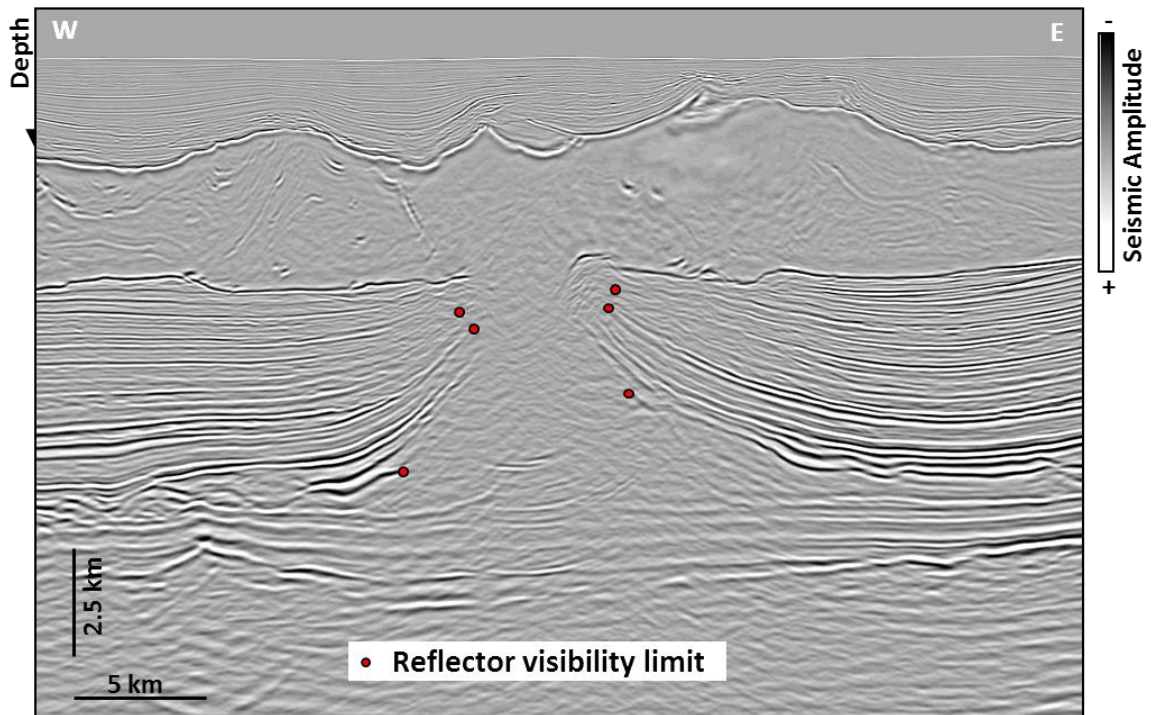


Figure 8 Field data RTM section showing the seismic visibility limits of the target horizons.

Figure 9 shows the comparison of the portion of W-E section through the center of the feeder overlain by the target horizon hit-count for the 8 km (a) and 14 km (b) maximum offset cases. Comparing the hit-count at each target, we can observe an

increase in the illumination in the flat-lying areas of the surface but negligible increase up-dip of the visibility limit.

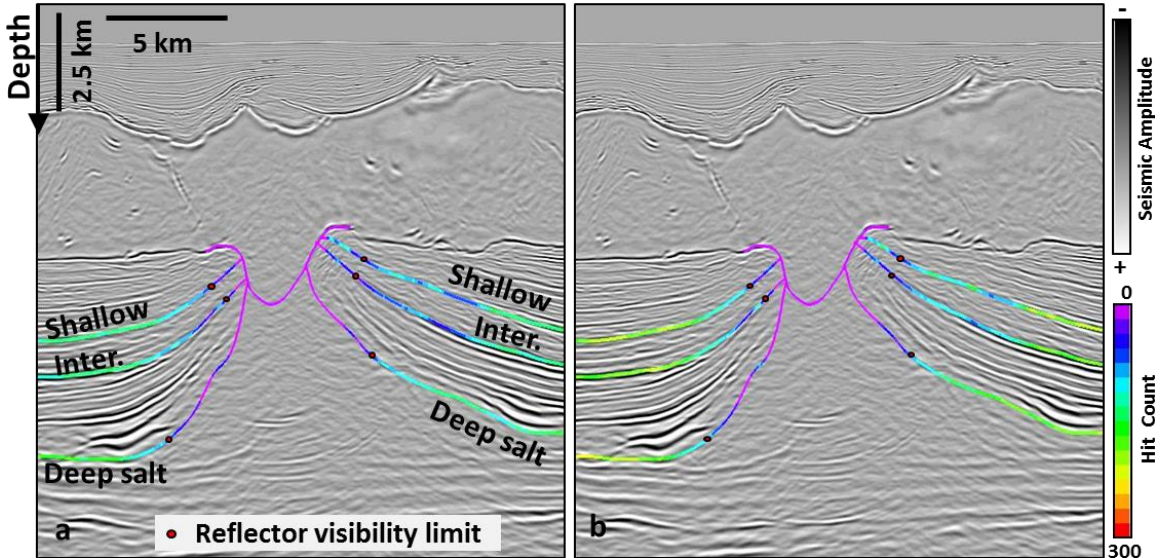


Figure 9 A comparison of seismic RTM image of field data overlain by hit-count for the shallow, intermediate and deep salt horizons using (a) 8 km maximum offset and (b) 14 km maximum offset geometry. The comparison shows increase in hit-count in flat lying areas of the targets but little to no increase in the hit-count of the areas up-dip of the reflector visibility limits.

The map views of the illumination results (Figure 10) show the strong correlation between low illumination zones (purple) and steep dips nearer to the center of the feeder. Comparison of the 0-14 km offset illumination maps (b, d, and d) with the 0-8 km case (a, c and e) for each of the three targets shows an increase in the illumination of the well-imaged flat-lying areas but shows only marginal increase in the poorly illuminated zones near to the salt feeder.

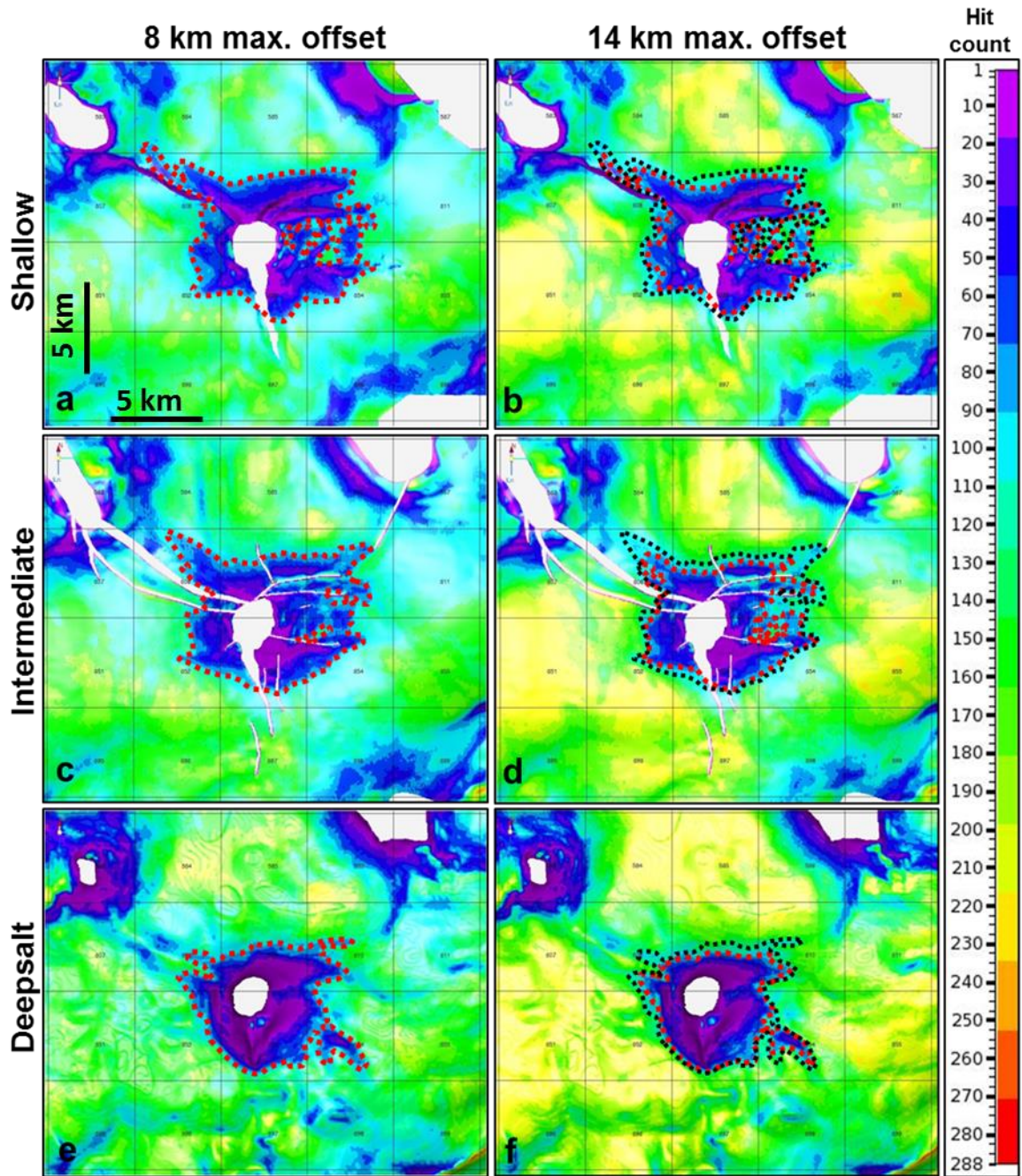


Figure 10 Common reflection point (CRP) hit-count maps for: (a) 0-8 km offset shallow target (b) 0-14 km offset shallow target (c) 0-8 km offset intermediate target (d) 0-14 km offset intermediate target (e) 0-8 km offset deep salt target and (f) 0-14 km offset deep salt target. Red outline represents the visibility limit interpreted from 0-8 km offset field data with a hit-count of approximately 75 hits. Black outline represents equivalent hit-count limit of 75 hits on the 0-14 km offset maps.

The red dashed outline on the maps represents the limit of reflector visibility for the 8 km offset case interpreted at a nominal hit-count of *ca.* 75 hits. Since the improvement in illumination is marginal, in order to highlight the change, the 8 km visibility limit was overlain on the 14 km illumination maps with a predicted visibility limit for the 14 km maximum offset case with a hit-count the same hit-count. The black outline shows the equivalent hit-count contour on the 14 km maximum offset illumination map.

Local illumination variations were observed on the shallow target (Figure 11). These variations are caused by undulations in the base of salt altering in the relative dip between the base of salt and the target structure. This effect is more significant with shallower subsalt targets and diminishes with depth. In deeper targets, the Fresnel zone is larger and therefore these targets are less sensitive to such short scale variations in geometry at the base of salt. Increasing the maximum offset smooths out these short scale length irregularities in the shallow subsalt target due to undershooting of the undulating base of salt. This is apparent when comparing the E flank of the shallow horizon beneath the rugose base of salt in Figures 9 a and b.

In this 3D CRP method, the parameterization was designed by using interactive ray tracing to determine the optimal ray cone opening angle from the flat-lying portions of the targets relative to the base of salt where illumination was expected to be highest.

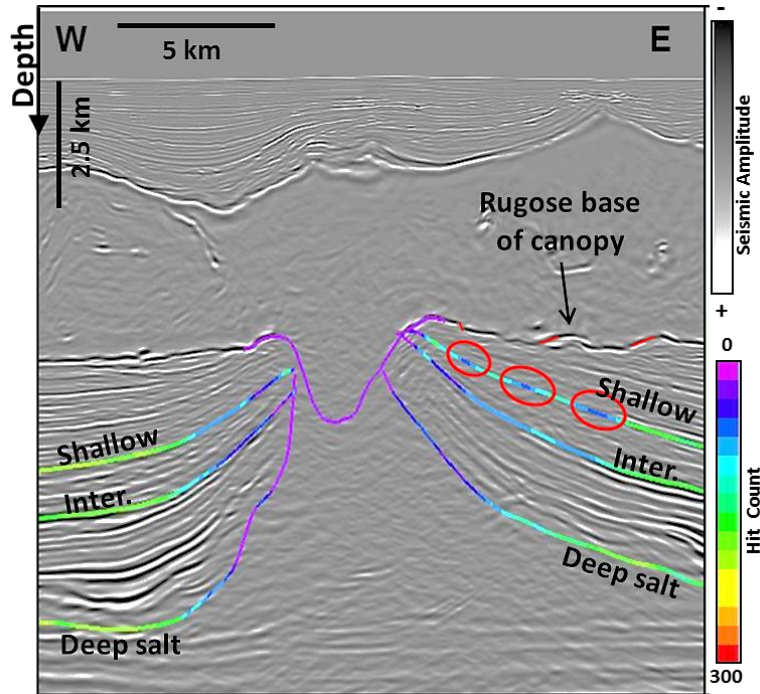


Figure 11 An enlarged view of the 8 km maximum offset illumination hit-count results encircling short wavelength illumination variations observed in the shallow horizon beneath the rugose base of salt canopy.

The caveat of this method is that it limits the subsurface opening angle to about  $36^\circ$  and therefore only considers the illumination of primary reflections on the target and is also limited by the inadequacies inherent to the ray tracing method in accurately representing the full-wavefield solution (See Section 1.2.3). The method described in this section uses hit-count maps as a proxy to represent illumination which is typically related to seismic amplitude. However, other factors affecting amplitude at the steep dip boundary should be considered, such as: the adequacy of the acquisition layout in terms of spatial coverage, azimuthal coverage and temporal sampling), changes in impedance contrasts along the surface due to rock property and fluid changes; non-primary P-wave reflections

such as prismatic waves, mode conversions and multiples; structural interpretation and velocity error and noise interference. Full-wavefield modeling is therefore recommended to better predict the contribution of longer offsets to the subsalt steep dip image.

## 2.2 Conclusions

The interactive ray tracing along with ray tracing illumination hit-count map computation were useful methods to illustrate the major factor affecting the illumination of the steeply dipping salt flank, *i.e.*, the post critical condition of reflections from the steep dip targets off of the base of salt canopy (Liao *et al.*, 2009). The comparison of ray tracing illumination hit-count between the 8 km and 14 km maximum offset cases showed marginal improvement in illumination of steep dips in the area where the signal to noise ratio is poor. Apart from the limitations of the ray tracing method inherent to ray theory, another critical caveat of this method of illumination analysis is that only primary P-wave illumination was modeled and omitted any illumination contribution from wider subsurface angle prismatic waves, mode conversions or multiples. In order to better predict the improvement of subsalt steep dip imaging in this case study, a more accurate full-wavefield modeling method is recommended.

## **Chapter 3 2D Acoustic forward modeling and RTM imaging**

The previous chapter showed that the ray tracing method has several limitations in accurately modeling wavefield propagation in complex media. This chapter discusses the more accurate full-wavefield modeling of synthetic acoustic data via 2D variable density acoustic finite-difference modeling (FDM) and subsequent RTM imaging with the objectives of validating the ray tracing illumination model and determining the effect of increased acquisition offset on the steep dip subsalt events.

### **3.1 Method**

A NW-SE 2D line (Figure 12) was selected from the 3D migration velocity volume. A 2D section of the velocity model used in the RTM migration of the RAZ field data the field data is shown in Figure 13. It shows complex features of the salt body including: rugose, high relief top of salt; the main salt feeder toward the SE; a nearby feeder NW of the main feeder; and a partially encapsulated mini-basin between the main salt feeder and a salt keel SE of the main feeder. In this method, synthetic seismic data is generated from interval velocity and density models using an acoustic, variable-density FDM algorithm and subsequently RTM migrated using the same velocity model used to generate the synthetic data.

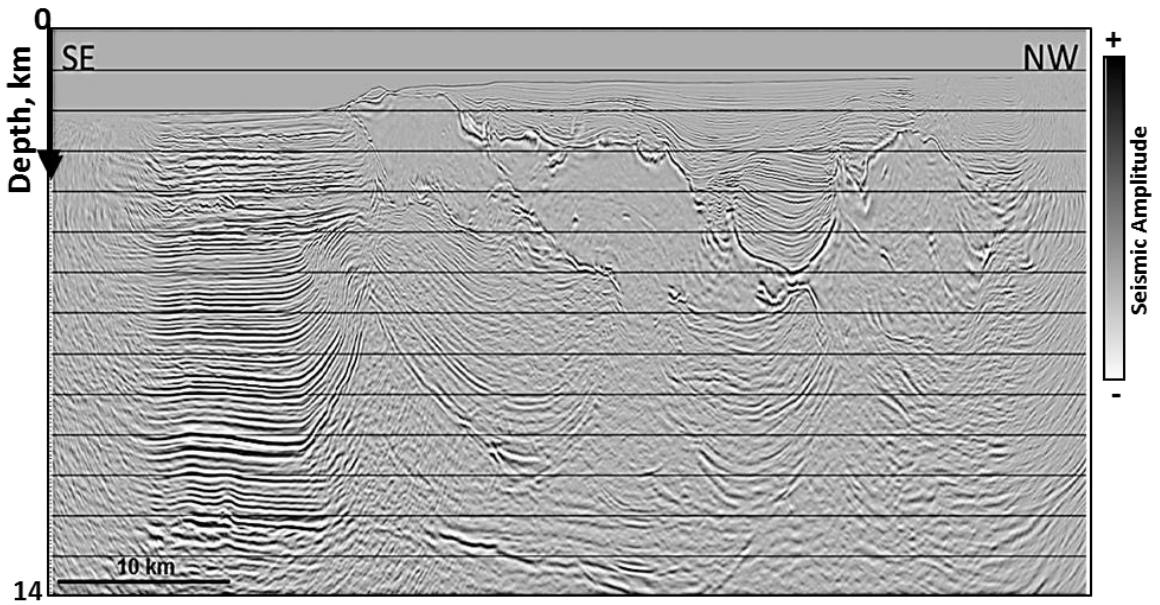


Figure 12 NW-SE 2D line section of the 3D field data RTM drawn through two salt feeders.

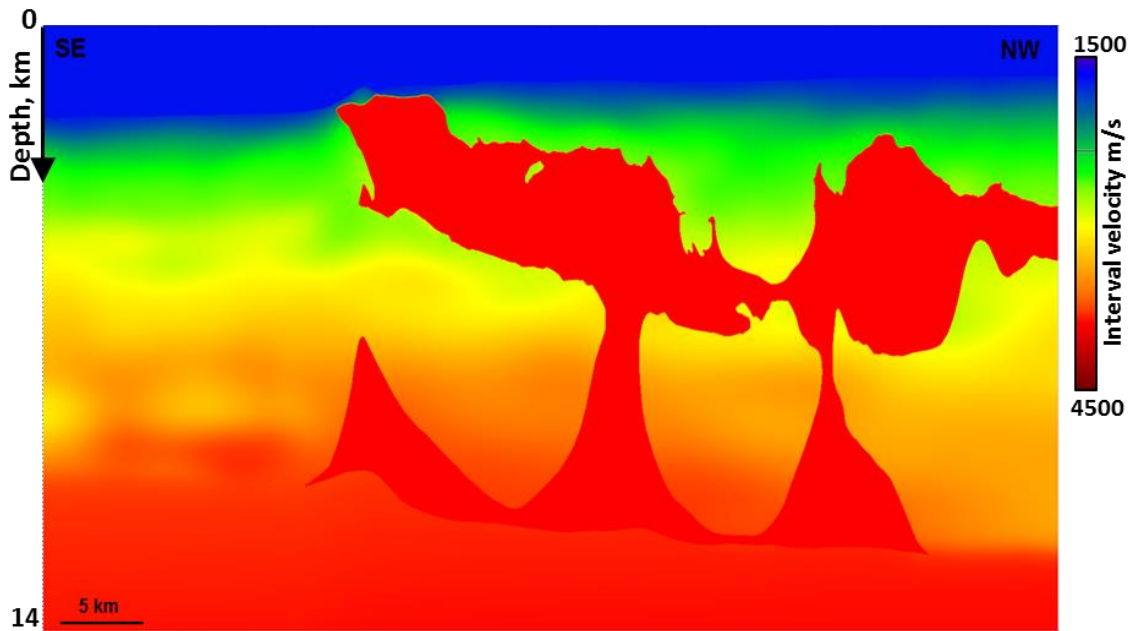


Figure 13 2D velocity model used as input for creating the FDM velocity model.

### 3.1.1 Acoustic FDM model building

The 2D variable density acoustic FDM algorithm requires a velocity and density attributes as input to generate synthetic reflection data. Density was derived from the Gardner equation (Gardner *et al.*, 1974) given by:

$$\rho = \alpha V_p^\beta, \quad (3)$$

where  $\rho$  is bulk density given in g/cc,  $V_p$  is P-wave velocity given in ft/s, and  $\alpha$  and  $\beta$  are empirically derived constants that depend on the geology. Gardner constants were derived from compressional sonic data (ft/s) and bulk density log data (g/cc) from four subsalt wells in the area.

Average values of 0.244 and 0.25 were obtained for  $\alpha$  and  $\beta$  and this equation were used to generate the background density model. The model includes five perturbation layers: at the water bottom; three subsalt layers (two of which correspond to the shallow and intermediate layers; and a pre-salt layer. Density contrasts of +5% were added to each layer in order to create the density contrast necessary for generating reflectors in the seismic forward modeling. The water layers and salt layers were given constant values of 1.03g/cc and 2.17 g/cc respectively (Figure 14).

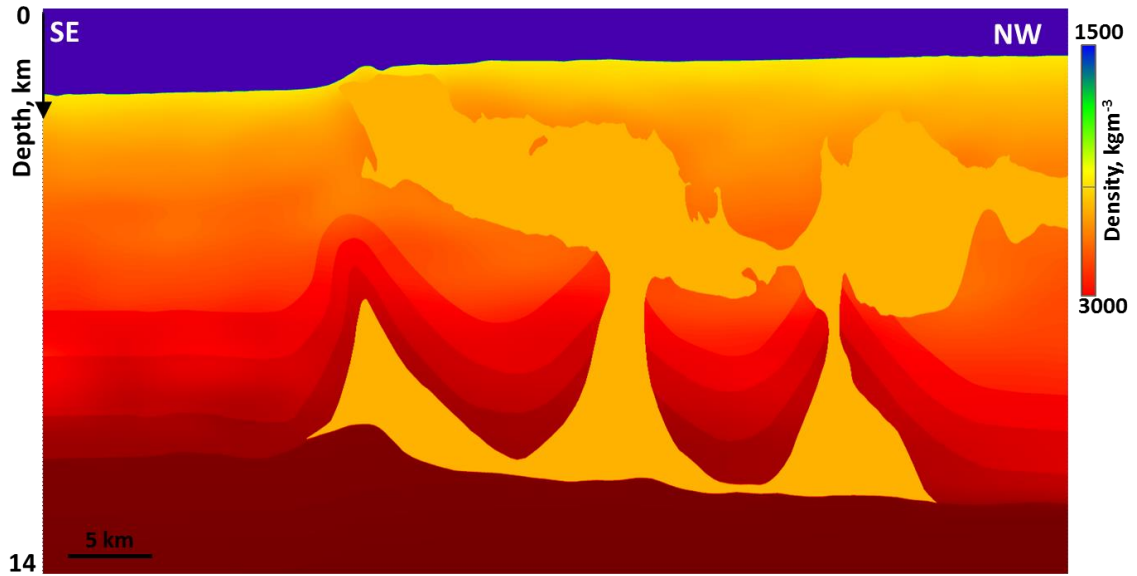


Figure 14 Density model built as input to the acoustic variable density FDM algorithm.

Details of the velocity and density model parameters used in the finite-difference modeling are listed in Table 2.

<b>Model Parameters</b>	
SRD	0 m
Maximum depth	14000 m
Depth interval	5 m
Number of vertical samples	2801
Total length	61,600 m
Lateral interval	5m
Velocity range	1490 – 4500 m/s
Density range	1000 – 3000 kg/m <sup>3</sup>

Table 2 Acoustic variable density input model parameters.

### 3.1.2 Acoustic forward modeling parameters

In FDM, spatial sampling is chosen to avoid grid dispersion in solutions. It is related to the shortest wavelength which must be modelled with sufficient accuracy. For 2D models, numerical dispersion is avoided when

$$dx \leq \frac{V_{\min}}{2 \times f \times dx \times n}, \quad (4)$$

where  $dx$  is the grid spacing in the  $x$  direction,  $V_{\min}$  is the minimum interval velocity in the model,  $f$  is the peak frequency of the source wavelet and  $n$  is the highest order of Taylor Series expansion upon which the finite-difference method is based. Figure 15 shows the dispersive effect of inadequate sampling rate in the direct wave.

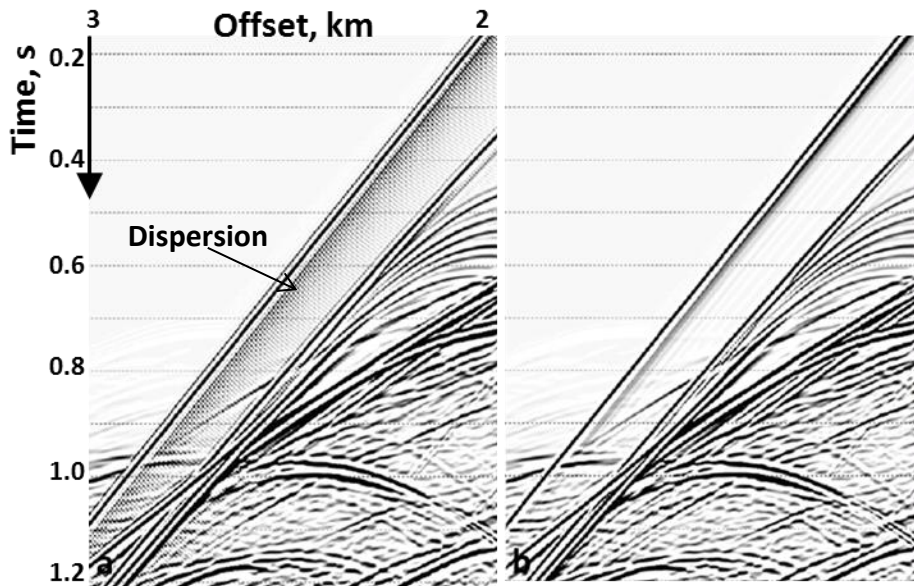


Figure 15 Synthetic seismograms showing (a) the effect of dispersion of the direct waves due to the spatial sampling interval failing to satisfy the dispersion criterion. (b) no dispersion due to the use of an appropriate sampling rate.

After selecting the minimum spatial sampling required, the time sampling is then determined by the stability criterion which gives the largest possible time step applicable for a numerical simulation of wave propagation in the given model (Table 3).

For 2D models, the stability criterion is satisfied when

$$\frac{V_{max} \times dt}{dx} \leq \frac{1}{\sqrt{2}}, \quad (5)$$

where  $V_{max}$  is the maximum interval velocity in the model,  $dt$  is the computation time sample and  $dx$  is the grid spacing in the x direction, (Lines *et al.*, 1999)

<b>Numerical Model Computation Parameters</b>	
Algorithm	Acoustic variable density finite-difference
Input datasets	P-wave velocity model, Density model
Grid size	$dx = dz = 5 \text{ m}$
Recording length	18 s
Time sample rate	0.5 ms
Output sample rate	4 ms
Number samples	4501
Source wavelet	Ricker
Dominant frequency	15 Hz

Table 3 Numerical modeling computation parameters.

The 2D source-receiver grid parameters were designed to model the bi-directional acquisition geometry with 8 km cable length and a hypothetical 14 km cable length in order to assess the effect of longer acquisition offsets on the image of the steeply dipping salt. Table 4 shows the source-receiver 2D line parameters defined in the acoustic finite-difference modeling.

<b>Source-Receiver 2D Line Parameters</b>		
SRD	0 m	
Range	0 – 61,600 m	
Shot interval	80 m	
Number of shots	771	
Cable length	8 km	14 km
Receiver interval	20 m	
Cable layout	Split-spread	

Table 4 2D FDM acquisition geometry parameters.

The FDM algorithm computes the 2D synthetic data in the common shot domain. In imaging, this data is directly used in the shot ordered domain as input into the RTM migration algorithm.

### **3.1.3 Imaging of synthetic data**

The 8 km synthetic data set and 14 km synthetic dataset were both migrated using an acoustic RTM migration algorithm and the same reference FDM velocity model and density models shown in Figure 13 and Figure 14, respectively.

The migration parameters used in each migration are as follows:

<b>RTM migration parameters</b>		
Algorithm	Acoustic RTM	
Input datasets	8 km offset synthetic shots	14 km offset synthetic shots
Maximum depth	14000 m	
Depth interval	10 m	
Migration aperture	14 km	17 km
Dominant frequency	15 Hz	
Source wavelet	Ricker	
Number of shots	771	
Shot interval	80 m	

Table 5 2D RTM migration parameters.

### 3.2 Results

This section shows the results of the FDM and subsequent RTM imaging of the 8 km maximum offset and 14 km maximum offset cases. For computational efficiency, the FD algorithm outputs the shot-by-shot solution to the wave equation and each shot can be visualized in several ways. The most common ways of representing synthetic shot data generated from wavefield extrapolation methods are via wavefield snapshots and seismograms or common shot gathers.

### 3.2.1 Wavefield snapshot

Wavefield snapshots graphically illustrate the generated synthetic data in the spatial domain at a particular instant in time. Scanning through wavefield snapshots gives the sense of wavefield propagation through the model. Figure 16 (a-f) show wavefield snapshots from a single shot location at 1.2, 1.8, 2.0, 3.0, 4.2 and 4.6 seconds respectively, overlaid on the reflectivity model generated from the velocity and density input models. Figure 16 (a) shows transmitted and reflected wavefronts generated from the shallow water bottom. The red and green lines at the top of each image represent the receiver cable layout for the shot represented by the yellow dot. The green line represents the 14 km maximum offset split-spread cable while the red line represents the 8 km maximum offset layout. At 1.2 s (Figure 16 a), only the direct wave has been recorded by the surface acquisition layout. Figure 16 (b) shows strong internal multiples generated at the shallow top of salt and reflected multiple times between the water bottom and the top of salt within just 1.8s of recording. Figure 16 (c) shows the interference pattern of the primary wavefield reflected off of the base of salt and the down-going first internal multiple. Figure 16 (d) shows the snapshot as the primary wavefield is reflected off of the deep top of salt. Figure 16 (e) and (f) show the snapshots at the points in time just before and after the primary wave impinges on of the steeply dipping salt flank respectively. Figure 16 (f) shows that most of the primary

energy is transmitted though the steep dip boundary with very little, energy reflected.

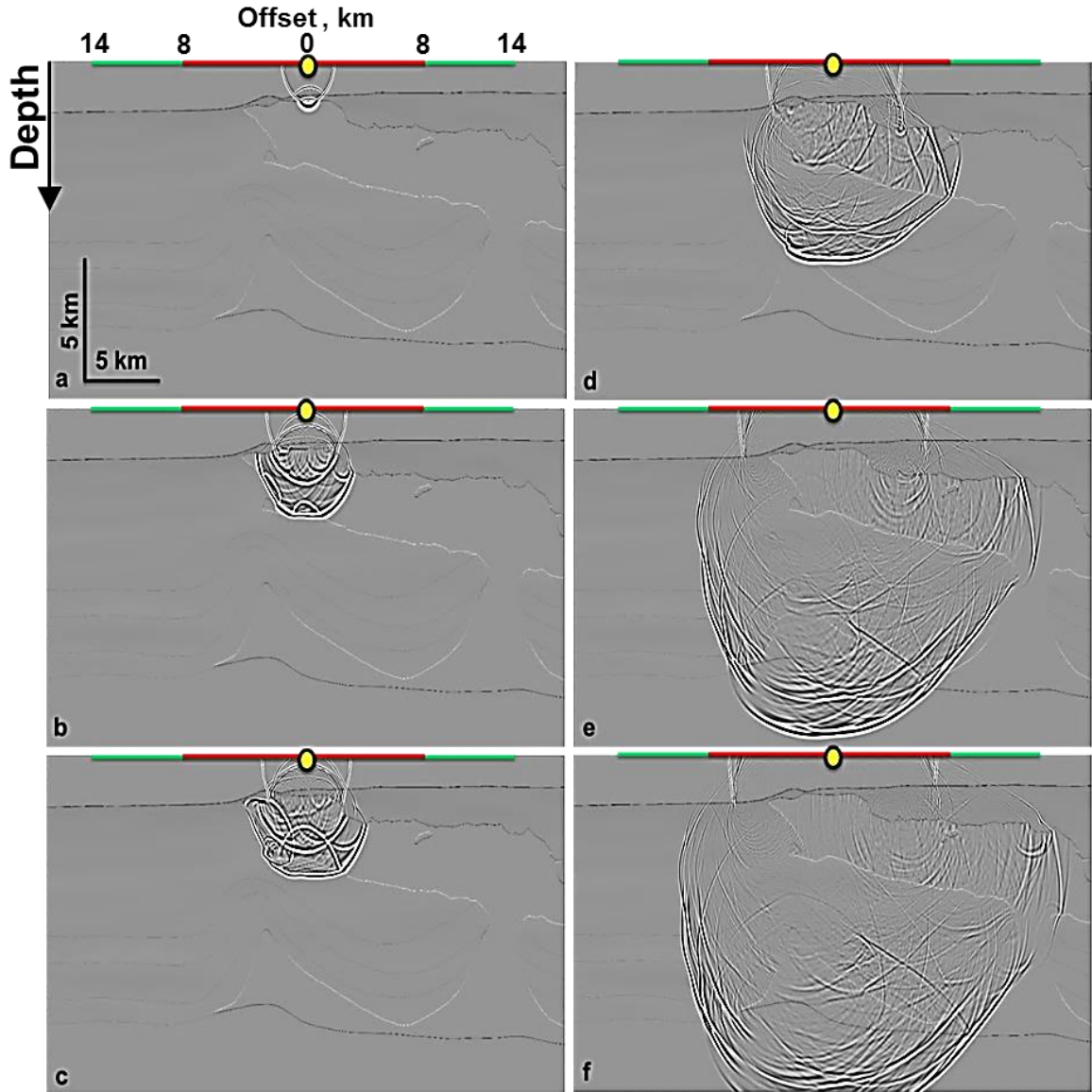


Figure 16 Synthetic wavefield snapshots generated from acoustic FDM. (a-f) show wavefield snapshots 1.2, 1.8, 2.0, 3.0, 4.2 and 4.6 seconds respectively, from a single shot located at location 17 overlaid on the reflectivity model generated from the velocity and density input models.

### 3.2.2 Acoustic synthetic seismogram

The seismogram or shot gather graphically represents the generated synthetic data in terms of source-receiver offset, amplitude and reflection time for a single shot location. Figure 17 shows an example of the seismogram computed using acoustic FDM for the same shot location illustrated by the wavefield snapshots in Figure 16 (a-f). The seismogram has a record length of 14 s and data with a maximum source-receiver distance of 14 km. The source-receiver split spread geometry for the 8 km and 14 km maximum offsets are represented by the red and green lines at the top of the seismogram respectively.

The shot location is shown by the yellow circle. The red box delineates the limit of the 8 km maximum offset data. At 8-9 s strong coherent energy is observed in the data extended to 14 km maximum offset that would be missing if only 8 km offsets were acquired. The source of the coherent events can be identified by looking at the 8-9 second wavefield snapshots and scanning back through time snapshots to identify their reflection location in the subsurface.

Although the interpretation of events observed in the shot record to the image may provide some information about the increased offset to the image; in a complex model, the energy is typically highly attenuated and interference patterns are too complex to identify the events for a single shot at longer offsets and later in the record. The best way to evaluate the contribution of longer offsets is in the

migrated stacked domain. The imaging of the data is discussed in the following section.

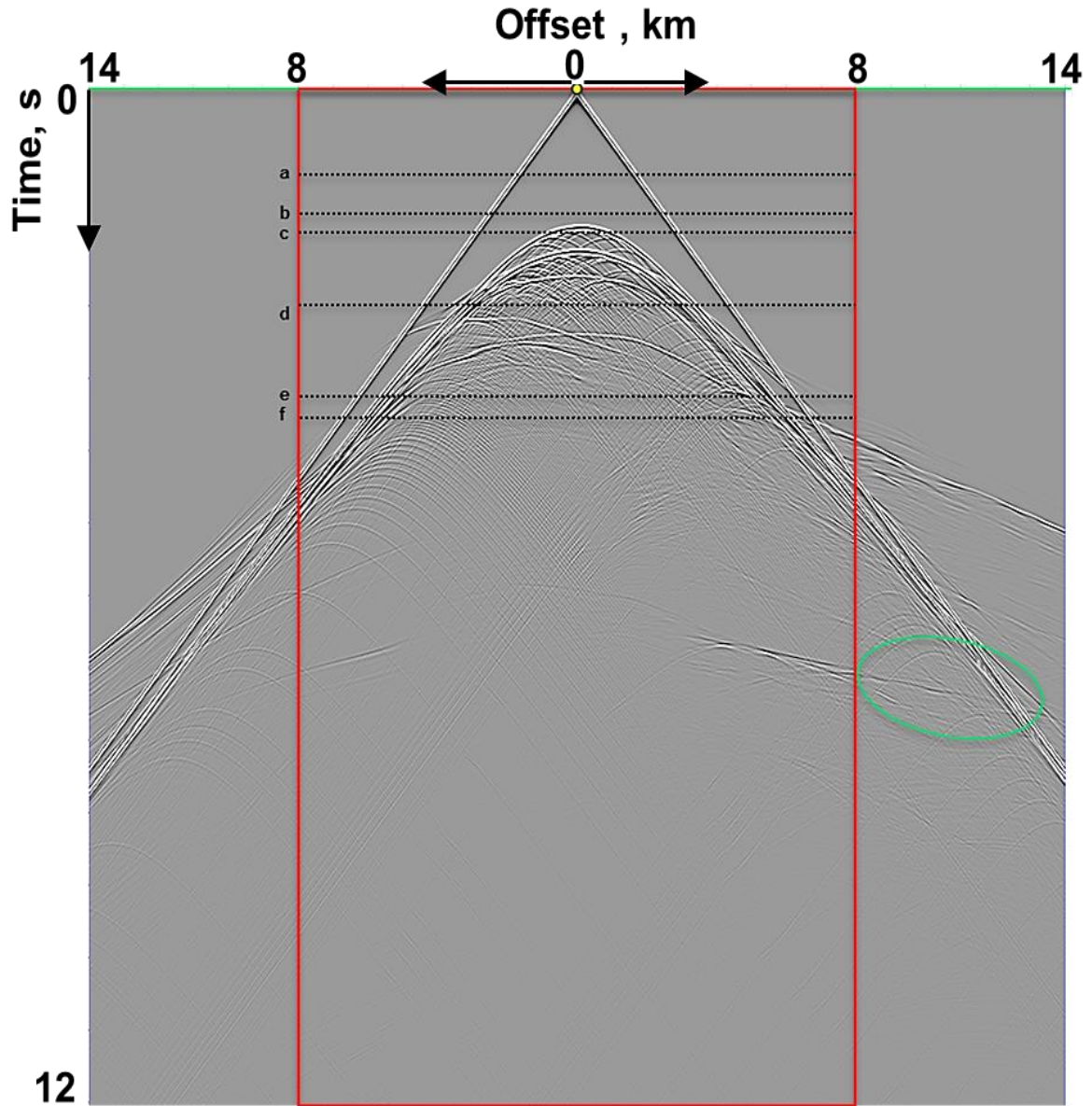


Figure 17 Synthetic seismogram computed using acoustic FDM for the same shot location illustrated by the wavefield snapshots in Figure 16.

### 3.2.3 RTM Imaging

Reverse-time migration was the preferred algorithm for imaging the synthetic data for several reasons: it is the most accurate imaging algorithm available to image pre-stack data, it has no dip-limitation and it allows significance of the conclusions drawn from this study to the implications for field RTM image.

The 8 km maximum offset and 14 km maximum offset datasets were individually migrated using the perfect velocity model and the results were compared in order to assess the contribution of the longer offset dataset to the image at the steep dip subsalt flank. For additional analysis, 0-8 km traces were removed from the 14 km dataset to produce a new pre-stack dataset with offsets of 8-14 km which was then migrated. This image directly shows the contribution of the longer offset data to the image.

The acoustic RTM algorithm computes the raw migrated stacked image and the Hessian source illumination matrix. The conventional cross-correlation imaging condition produces strong low-frequency migration artifacts in RTM generated by the cross correlation of reflections, back-scattered waves, head waves and diving waves. The artifacts are reduced using a Laplacian filter to the stacked image without affecting the steep dip reflections (Zhang and Sun, 2009). Figure 18 shows the raw RTM migrated stacked image pre-Laplacian filtering with strong back-scatter noise above the shallow salt. The Laplacian filter causes a 90° phase shift

because it is a second order differential. This polarity flip can be observed when we compare the raw RTM (Figure 18) with the Laplacian filtered image (Figure 20). The Hessian matrix of the migration operator contains the source illumination information and can be used to compensate seismic amplitudes for transmission losses during wavefield propagation in the subsurface, (Tang, 2008). The Hessian matrix can be obtained by taking the second derivative of the objective function with respect to the model parameters and represents the curvature of the least squares objective function. Figure 19 shows the source illumination computed from RTM migration.

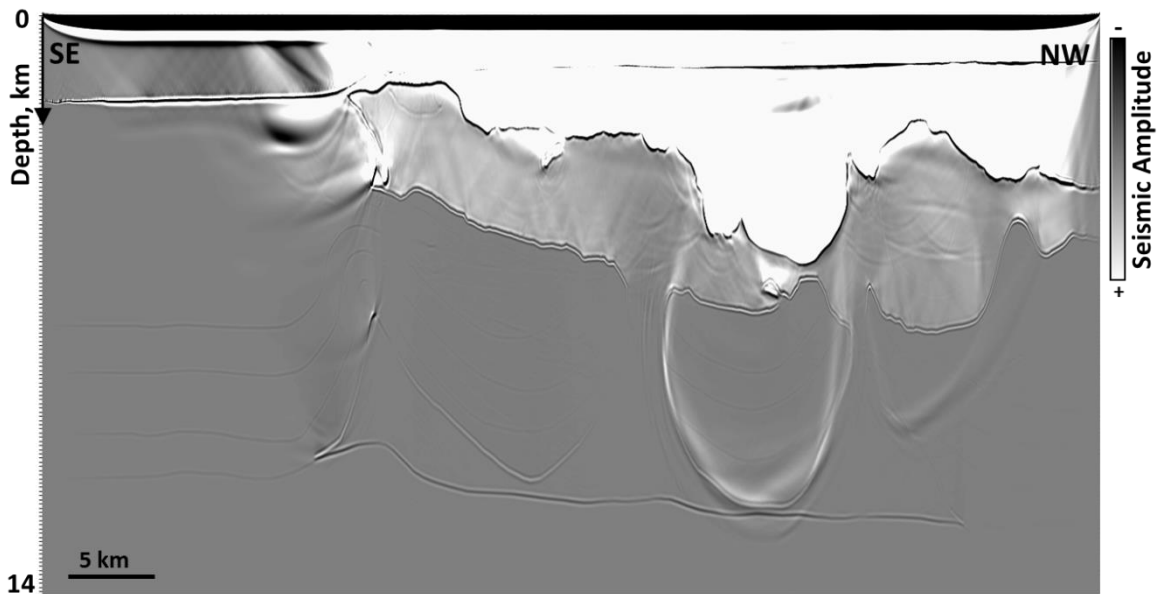


Figure 18 RTM raw stack of synthetic data, before the Laplacian filter is applied, showing strong positive amplitude back-scatter noise in white above the shallow salt and along the boundary of the encapsulated mini-basin.

The synthetic data generated from the 2D variable density acoustic finite-difference modeling of data with (a) 0-8 km offset, (b) 0-14 km offset and (c) 8-14

km offset data were RTM migrated with the model in Figure 13 to give the results shown in Figure 20, Figure 21 and Figure 22 respectively.

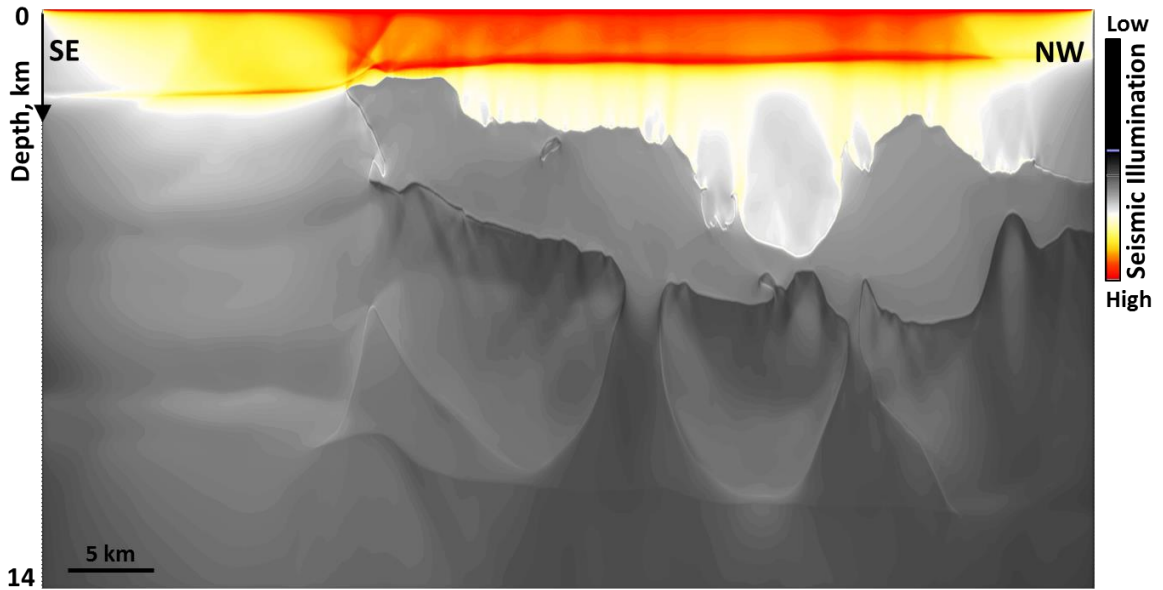


Figure 19 Source illumination computed from the RTM algorithm. Red color represents high source illumination decreasing to black.

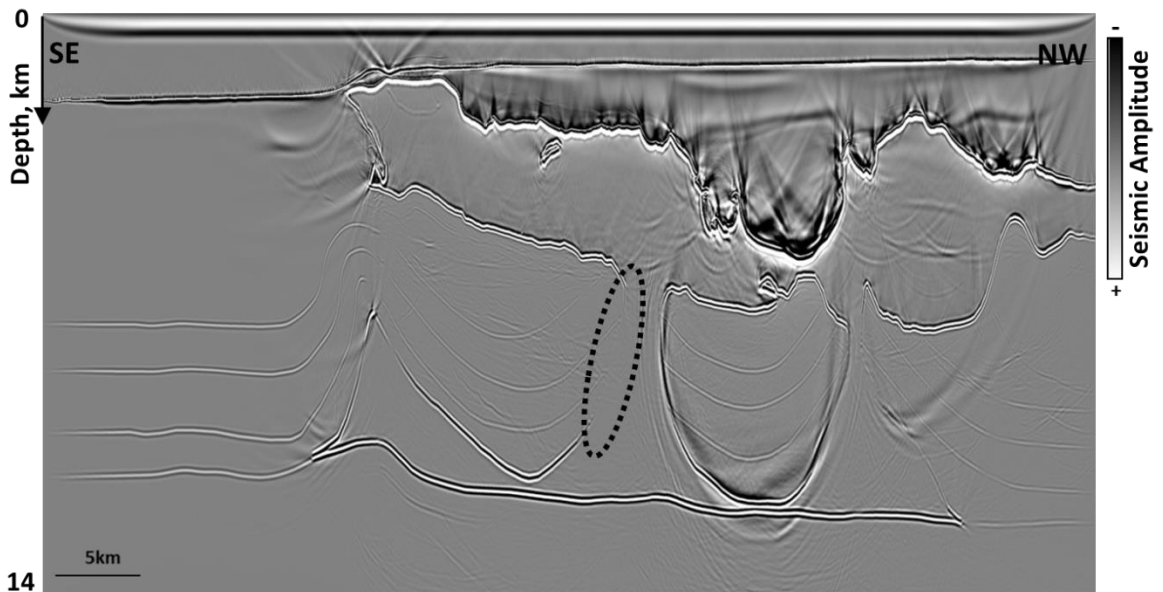


Figure 20 Laplacian filtered RTM migration stack of 0-8 km offset synthetic data. Encircled area shows no image of the SE flank of the main feeder.

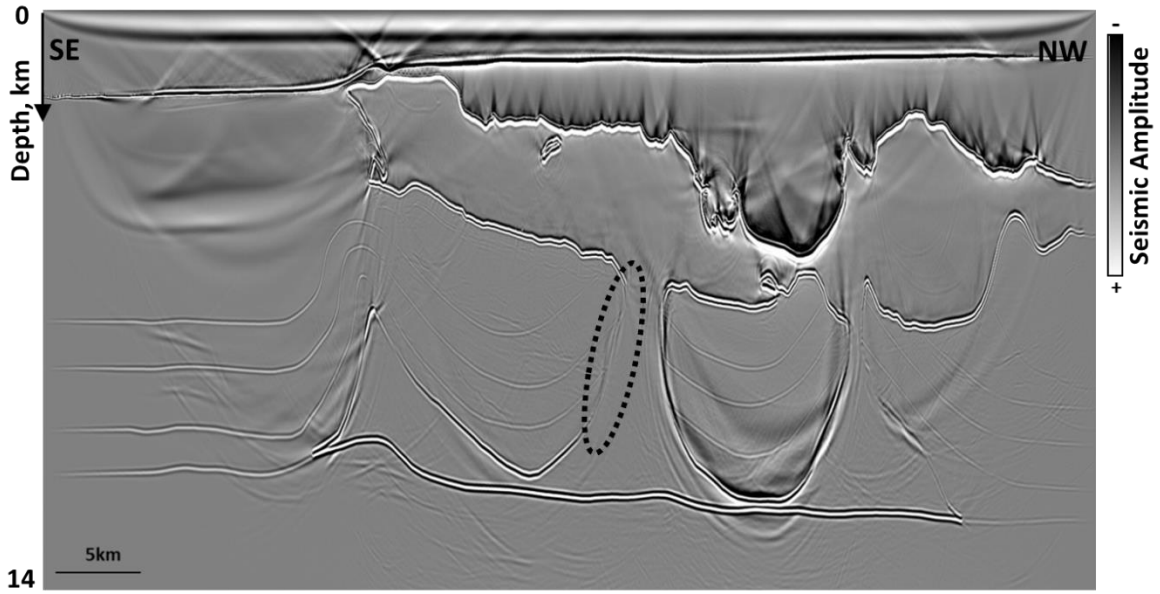


Figure 21 Laplacian filtered RTM migration stack of 0-14 km offset synthetic data. Encircled area shows an increase in coherent amplitudes of the steep SE flank of the main feeder compared to the image of the 0-8 km data.

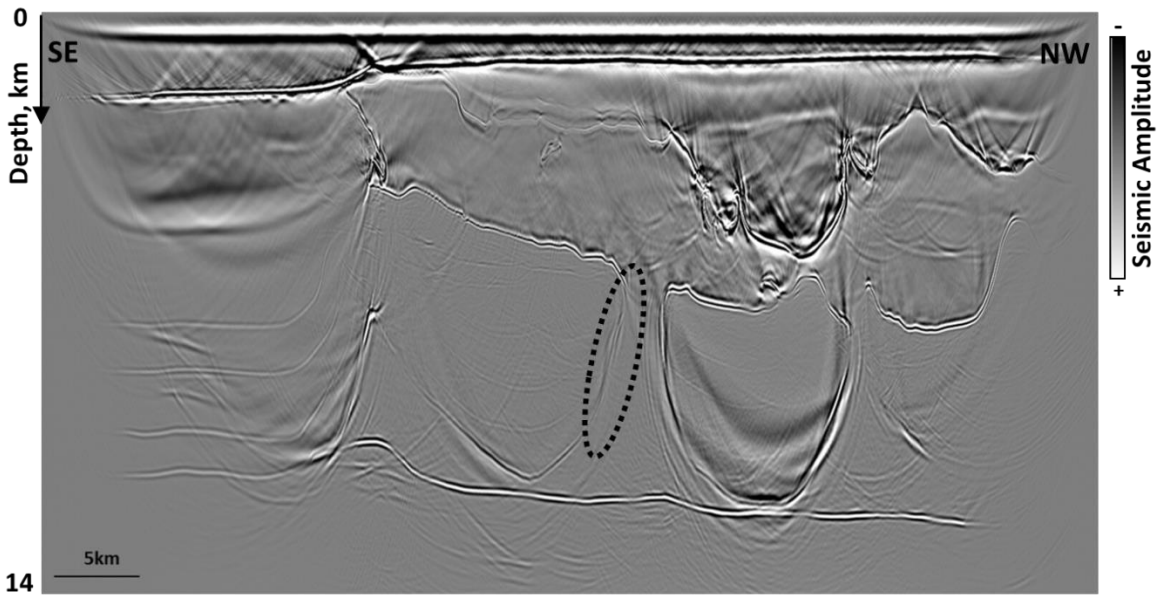


Figure 22 Laplacian filtered RTM migration stack of 8-14 km offset synthetic data. Encircled area shows that all of the coherent energy from the steep SE flank of the main feeder is contributed by 8 – 14 km offset data.

### 3.3 Discussion

In the RTM image of up to 8 km maximum offsets, the SE steeply dipping flank of the salt feeder was not imaged at all. Figure 20 highlights the steep dip subsalt target of the SE dipping flank of the main feeder. The poor image of this target is consistent with the low illumination shown on the 8 km maximum offset ray tracing illumination map of the deep salt horizon in Figure 10e. However, the NW dipping flank of the main feeder and the SE dipping flank of the secondary feeder are both well imaged even with up to 8 km offset contrary to the ray tracing illumination map. This is due to illumination from prismatic waves. Full-wavefield modeling and imaging methods provide a natural way to image prismatic waves (Zhang and Sun, 2009, Farmer *et al.*, 2006) and also has the potential to image multiples if all of the reflector generating boundaries exist in the model used to predict the multiple events.

#### 3.3.1 Imaging with prismatic reflections

Comparison of the RTM image of the synthetic data with 0-14 km offsets (Figure 21) and 8-14 km offsets (Figure 22) shows improvement in the image of steeper dips on the SE flank of the feeder, when compared the 0-8 km offset case. Low frequency RTM artifacts can also be observed in the longer offset migrated data.

This could be explained by the increased offset and aperture including energy scattered further out through the model as prismatic waves and far offset turning

waves undershooting the salt. A closer look at the low frequency artifacts generated by the RTM (Figure 22) reveals the prismatic path that illuminates the SE steep dip flank (Figure 23).

These beams are also visible in the source illumination profile where the dip in the base of salt is towards the dip direction of the salt feeder. This base of canopy geometry combined with the shape of the deep top of salt provides a localized window for the prismatic waves to illuminate the salt flank (Figure 24). The prismatic wave path that illuminates the attic region of the main flank is captured by the 0-14 km offset geometry, but the 0-8 km offset geometry appears insufficient to capture the prismatic energy.

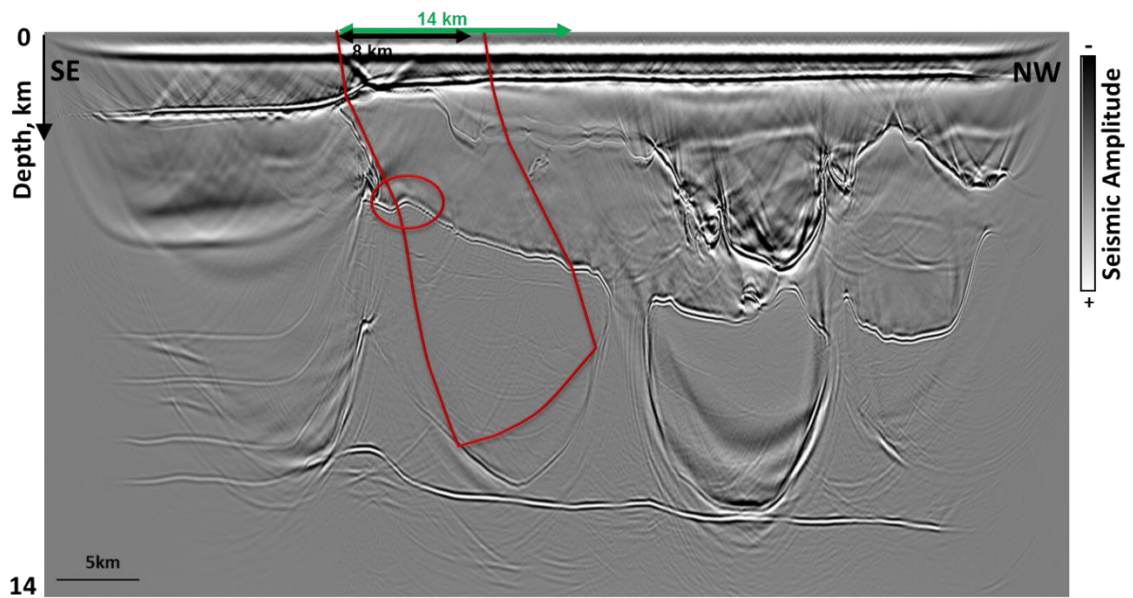


Figure 23 RTM migration stack of 8-14 km offset synthetic data showing the raypath of prismatic waves reflected through the illumination window created by the small-scale concave anomaly (encircled) at the base of salt canopy and off of the steeply dipping salt feeder.

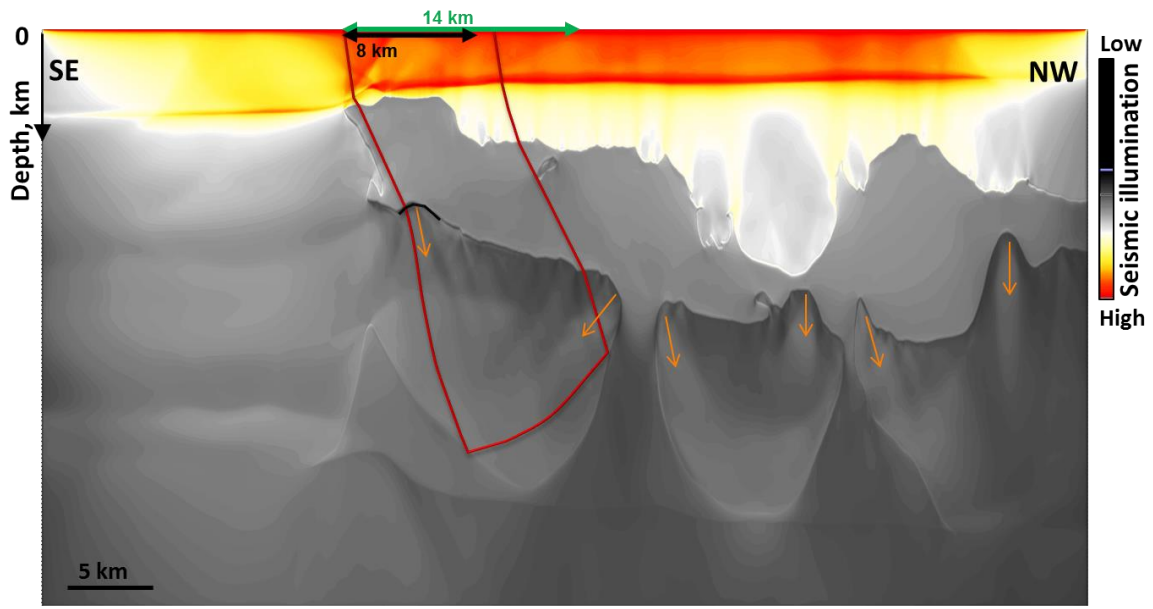


Figure 24 Source illumination matrix showing illumination windows observed at six locations due to the concave structure of the base of salt. Red color represents high source illumination decreasing to grey. The prismatic raypath reflected off of the SE dipping flank of the main salt feeder is traced in red. Black and green arrows at the surface represent the 8 km and 14 km offset source-receiver spread respectively.

Each of the locations indicated by the orange arrows in Figure 24 shows a concave shaped base of salt and the illumination windows associated with these localized base salt canopy undulations. The windows allow beams of energy to penetrate through the salt increasing the illumination of events in their path. The orange arrows show the approximate axis of the illumination beams from each of the identified windows.

The concave base outlined in Figure 24 focuses the prismatic waves reflecting off of the underlying salt keel toward the SE dipping steep flank thereby enhancing the effect of the additional offset and aperture in this particular case.

The NW-dipping flank of the main feeder and the SE dipping flank of a nearby feeder toward the NW are both well imaged in the 0-8 km case (Figure 20) because shape of the base of the mini-basin, which is completely enclosed by salt (in 2D) allowing the prismatic waves to be reflected off of all angles within the 2D plane. Figure 25 shows a prismatic raypath reflected between the feeders off of both steeply dipping flanks of the encapsulated mini-basin and being recorded within both the 14 km maximum offset and the 8 km maximum offset geometries. Illumination may also increased at this location by the depression in the top of salt canopy causing relatively thinner salt.

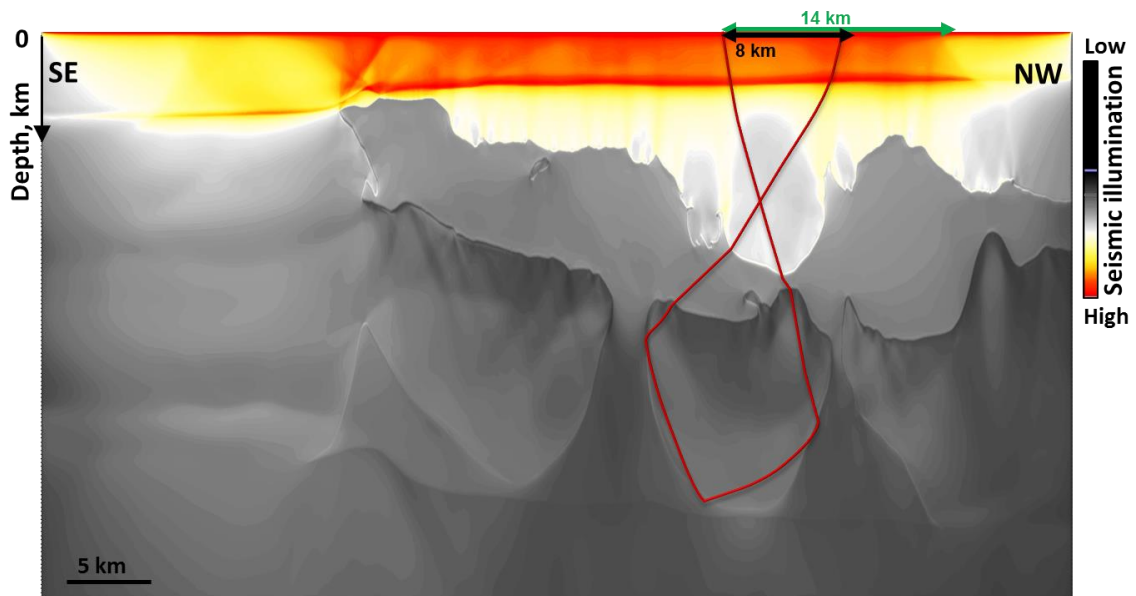


Figure 25 Source illumination matrix showing illumination windows observed at six locations due to the concave structure of the base of salt. Red colors represent high source illumination decreasing to grey. The prismatic raypath traced through the enclosed mini-basin between the two feeders is highlighted. Black and green arrows at the surface represent the 8 km and 14 km offset source-receiver spread respectively.

The contribution of prismatic waves depends on the structure of the bodies allowing multiple reflections, such as the deep top of salt in this case. A concave shape of the top of deep salt focuses prismatic waves on to the steeply dipping portion of the feeder. This effect is magnified at the boundary of the enclosed mini-basin imaging all dips due to the high concentration of prismatic reflections (Figure 25). Imaging with prismatic waves requires very accurate definition of the salt geometry and subsalt velocities. The uncertainties in the velocity model and noise in the data may reduce the significance of the contribution to the image of the actual field data.

Imaging with multiply reflected waves has shown to be beneficial for improving the illumination beneath complex salt due to the large variety of raypaths traveled by the multiples and the smaller angle range of multiply reflected waves (Liu *et al.*, 2011). Imaging with multiples can be done by treating the multiply reflected energy as primary energy and migrating the multiples using conventional imaging methods (Verschuur and Berkhout, 2005).

### **3.3.2 Undershooting**

Li *et al.*, (2014) attributed the extra illumination for subsalt events under complex salt structures to the undershooting of the overlying salt complexity. Altering the ray parameters and shooting from the steeply dipping flank toward the edge of the salt canopy with sufficiently long aperture allows increased illumination due to at

least one leg of the successful ray pair undershooting the salt, even with 8 km offset (Figure 26 and Figure 27). This particular salt body has an extensive salt canopy with an average thickness of 2.5 km however, increased illumination can occur due to at undershooting of the canopy by at least leg of the ray pair. At the shortest distance from the salt feeder to the edge of the salt canopy, the migration aperture required to capture rays successfully reflected off of the tested location on the steep dip interface is at least 25 km, which is impractical for imaging the entire dataset, but targeted RTM imaging of the shots that illuminate the steep dips may prove advantageous.

Ray tracing with unlimited aperture can help to identify opportunities for locally improving the zones of poor illumination followed by the migration of only the shots that illuminate these targets. This selective reduction in the volume of data can allow larger apertures to be migrated, and improve the illumination of the steep dips.

We have seen that increasing the acquisition offset can improve the steep dip image due to the acquisition of more prismatic waves and energy undershooting the edge of salt. In order to further distinguish the contributions to the steep dip image of undershooting compared to prismatic wave imaging, the synthetic data was migrated with a model having removed the deep salt layer leaving only the shallow salt canopy layer in the model (Figure 28).

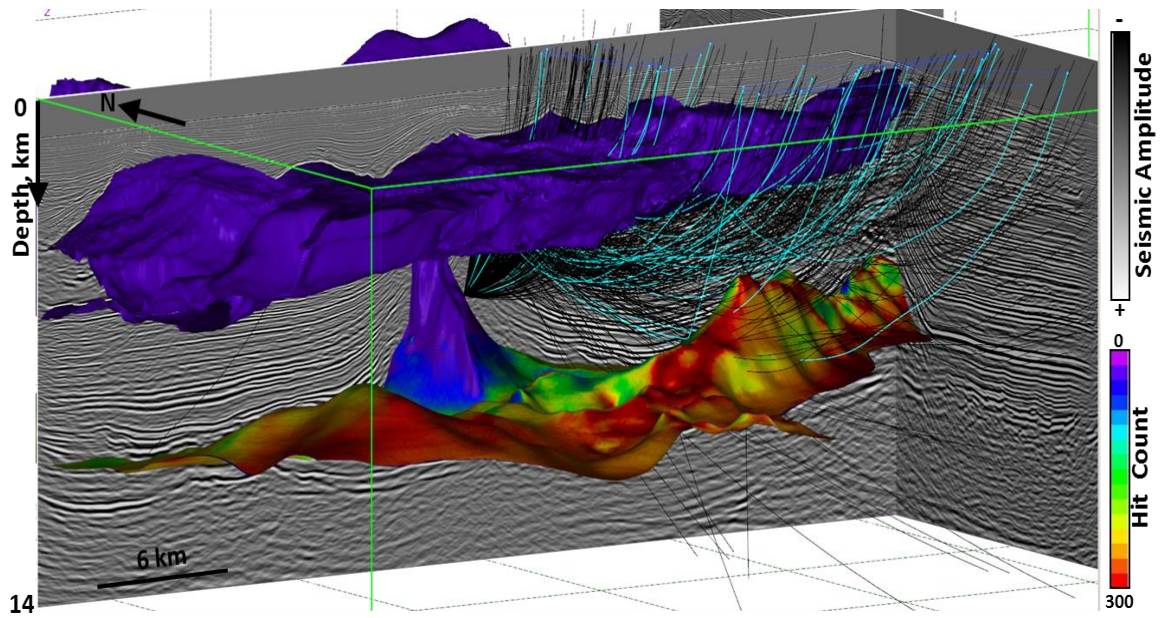


Figure 26 3D view showing the salt canopy structure (dark purple) and failed (black) and successful rays (light blue) undershooting the canopy from the steep dip flank. The ray cone is shot from the deep salt surface displaying the hit-count through the RTM seismic field data displayed in the background sections.

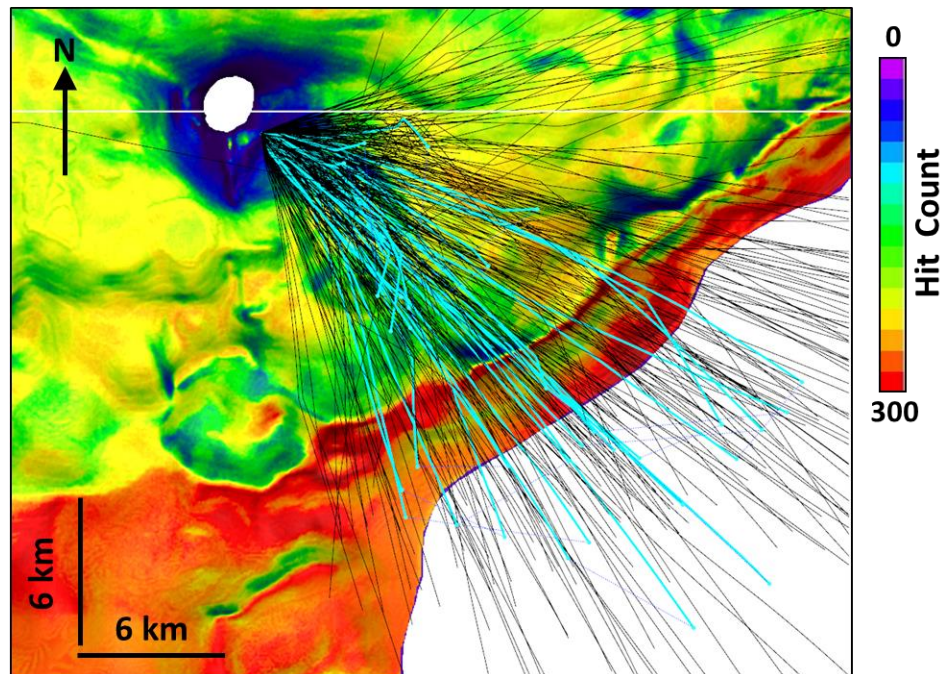


Figure 27 Map view of hit-count on deep salt surface with failed (black) and successful rays (cyan) undershooting the canopy to the edge of the Sigsbee escarpment (red area).

Without the deep salt layer to reflect the prismatic waves the target steep dip SE flank is not imaged at all in the 0-8 km offset case (Figure 29). This proves that the imaging of prismatic waves has a significant impact on the imaging of steep subsalt dips. However, migrating the 0-14 km offset synthetic data with the canopy-only velocity model shows some contribution to the up-dip region of the SE flank. This suggests that undershooting the edge of salt is possible by increasing the maximum offset to 14 km (Figure 30).

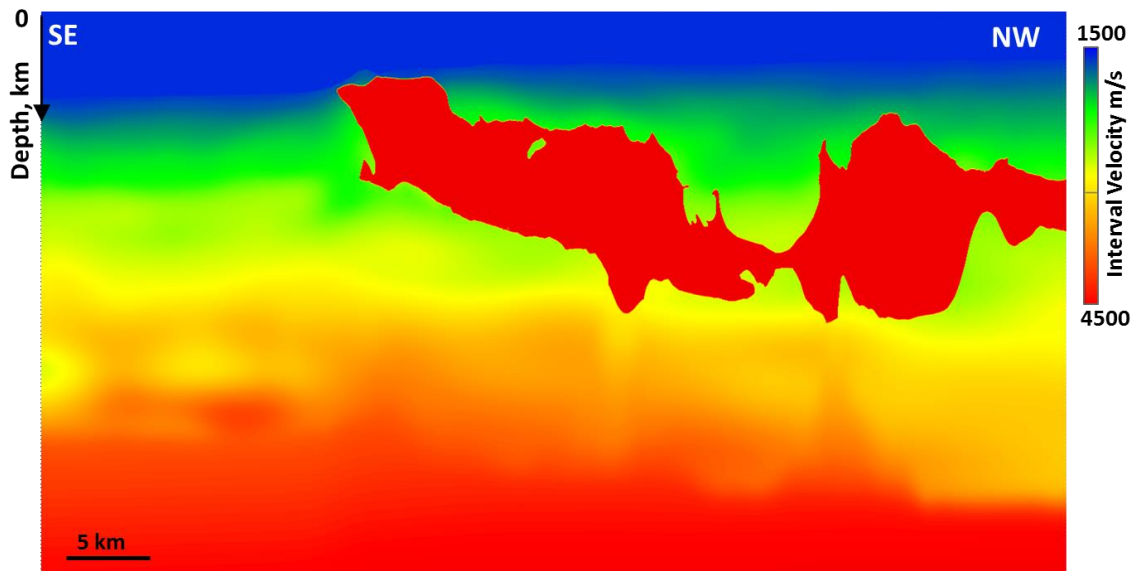


Figure 28 2D velocity model with deep salt layer replaced with background sediment.

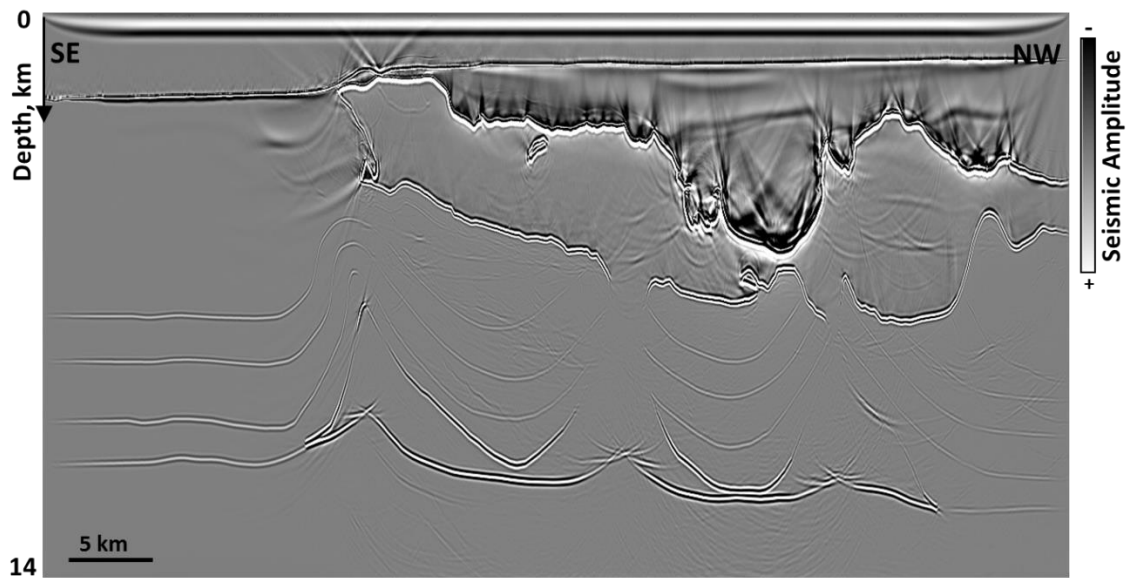


Figure 29 RTM migration stack of 0-8 km offset synthetic data using the velocity model with salt canopy only.

These results suggest some potential for the longer offset data to improve the subsalt illumination holes caused by steep dips. Since the behavior of prismatic waves is highly dependent on the geometry of the reflecting surface.

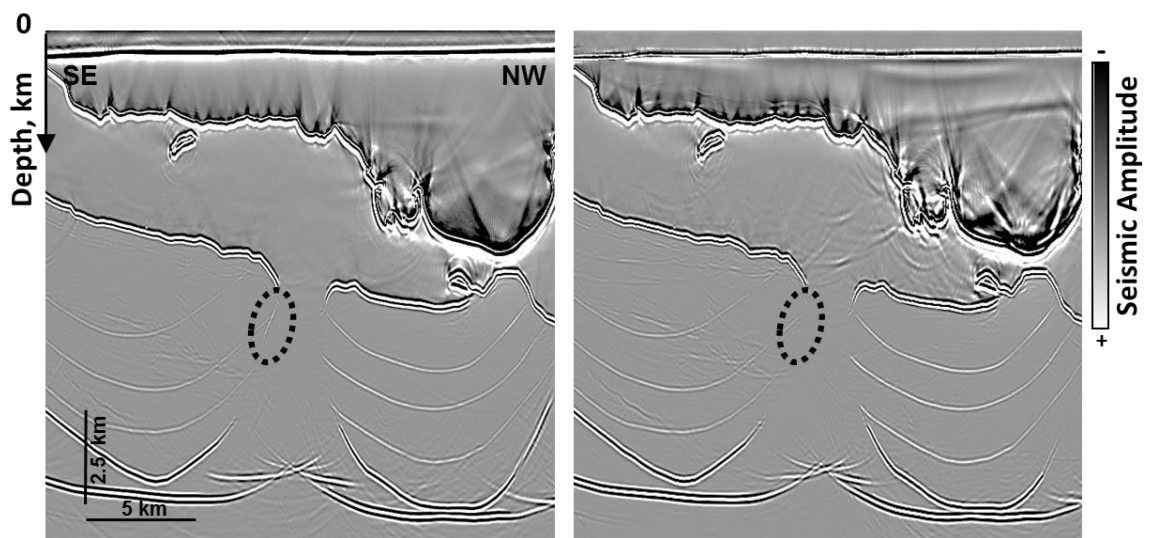


Figure 30 RTM migration stacks of (a) 0-8 km offset data and (b) 0-14 km offset data migrated using the velocity model with salt canopy only.

In this case, increasing the offset to 14 km showed improvement in the steep-dip image, but this may not have been the case if the deep top of salt were flat rather than synclinal. The minimum offset and travel-time required to image these waves can be predicted by modeling with a sufficiently accurate velocity model.

Improvement in the steep dip subsalt illumination by imaging prismatic waves is also highly dependent on the accuracy of the model and in practice; the model may not be sufficiently accurate to image the non-primary energy. Another consideration that must be taken into account is that although the top of seep salt geometry focuses these prismatic waves toward the steep dip attic region within 14 km offset, this may not be the case in 3D. It is recommended to extend this study to 3D in order to more accurately the effect of longer offsets on the steep dip image.

### **3.3.3 Amplitude and illumination**

Illumination it is not the only factor affecting subsurface amplitudes. There are five major independent causes of poor signal-to-noise ratio in the subsalt image. These are: illumination; rock properties; non-primary P-wave reflections such as prismatic waves, mode conversions and multiples; earth model error and algorithm bias. In theory, a boundary with no contrast in impedance would not produce a reflection even if fully illuminated. A variable density algorithm was used to generate the reflections therefore illumination and rock property effects on the

amplitude are coupled in this experiment. An acoustic impedance model (Figure 31) was generated from velocity and density models (Figure 13 and Figure 14).

From this, P-wave reflectivity ( $R_{PP}$ ) was computed from top-down with a simple formula:

$$R_{PP} = \frac{a_{n+1} - a_n}{a_{n+1} + a_n}, \quad (6)$$

where  $a_n$  is the acoustic impedance of sample n, and  $a_n$  is the acoustic impedance of the subsequent sample. Figure 31 shows the resulting acoustic impedance section. The contrast in acoustic impedance decreases to a minimum creating a nearly acoustically transparent zone in the  $R_{PP}$  section at around 8.5 km depth with an extent of about 500 m (Figure 32).

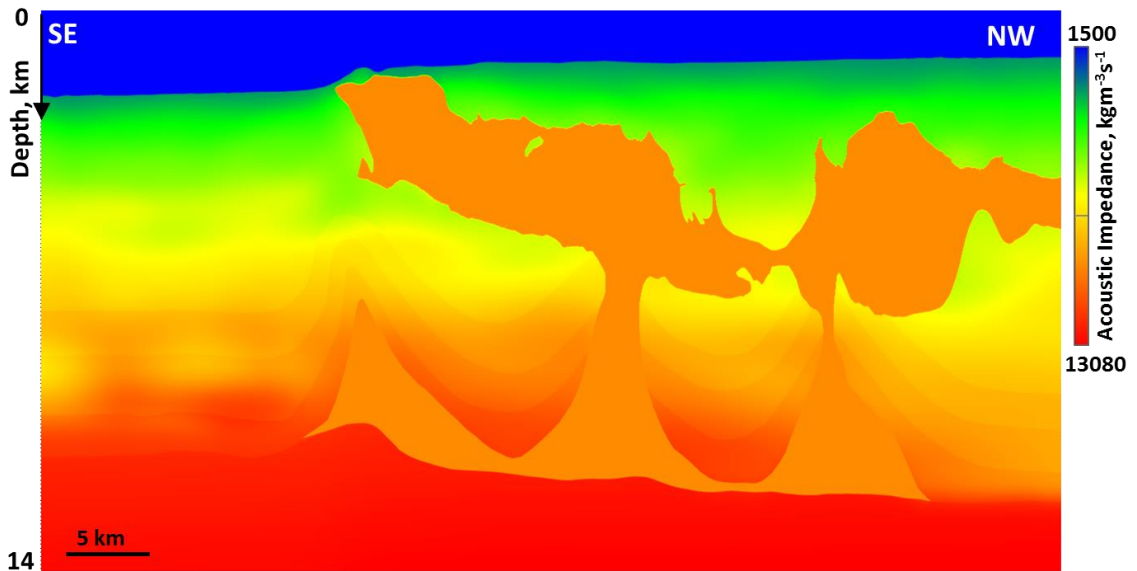


Figure 31 Acoustic impedance section computed from acoustic FDM input velocity and density models.

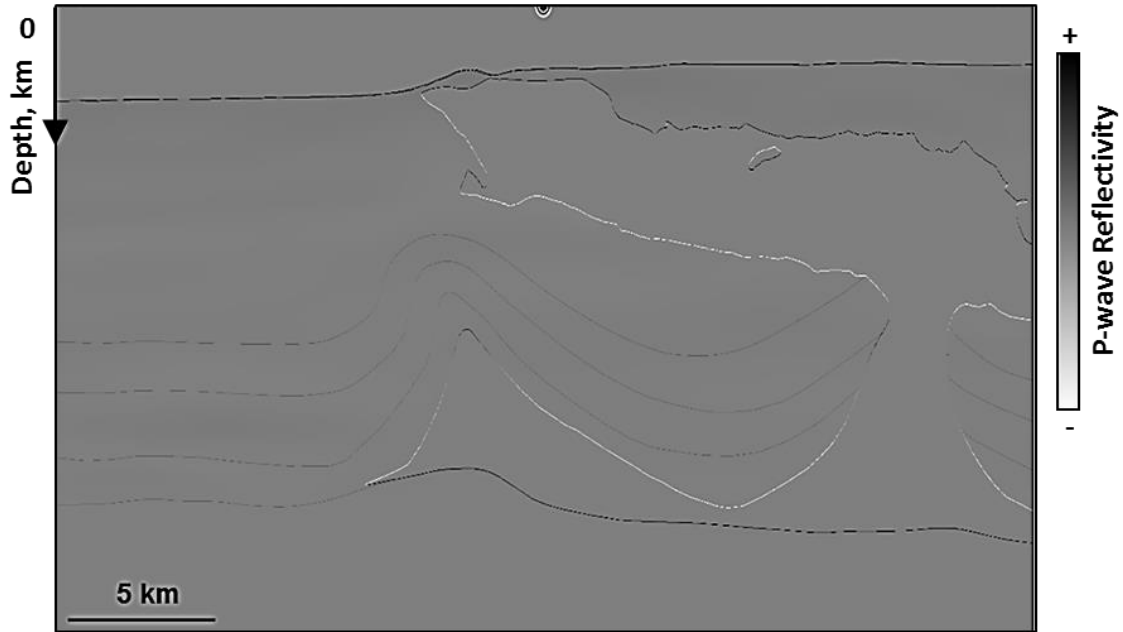


Figure 32 A P-wave reflectivity section computed from acoustic impedance volume. Black represents high positive reflectivity and white represents high negative reflectivity.

The poor image of the 8 km maximum offset FDM RTM of the SE dipping flank extends from *ca.* 6.5 km to 10 km (Figure 20) and is only locally affected by an acoustically transparent zone. In this case, the acoustically transparent zone cannot account entirely for the poorly imaged salt flank, however this needs to be considered when evaluating the impact that increased illumination would have on the image.

### 3.4 Conclusions

I demonstrated that longer offset and apertures were able to increase the illumination of the steep subsalt dips by capturing the prismatic waves using

longer offset acquisition geometry. The combination of increased offset and aperture capturing prismatic waves; and the focusing effect of the concave base of salt facilitated improvement in the illumination of the steep dip subsalt target within 14 km maximum offset in this specific case. In ray tracing analysis, parameterization specific to high-reflection angle prismatic waves, is recommended to evaluate the contribution of this type of energy to steep dip illumination.

This 2D modeling case study illustrates the importance of imaging prismatic waves; and long offset salt-canopy undershooting; to imaging steep dips but is inconsistent with the image of the steep dips in the field data specifically in the area between the two feeders (Figure 18). This 2D FDM study does not account for the 3D variations in the subsurface illumination and therefore a 3D modeling study is required to effectively determine the extent to which increasing acquisition offset will benefit the image.

## **Chapter 4 Converted-wave forward modeling and imaging**

The application of converted waves in imaging beneath high velocity layers such as salt canopies has proven to be beneficial for increasing illumination of steeply-dipping events in several studies (see Section 1.2.7). This chapter describes the elastic full-wavefield modeling and imaging method used to assess the impact of converted wave illumination using a simplified salt canopy-feeder model. First I describe how the model is built, followed by the parameterization of the elastic FDM algorithm and discuss the results of the image comparing the acoustic imaging with converted wave imaging.

### **4.1 Method**

In this section, I investigate the potential of using converted waves to improve steep dip illumination on a geometrically simplified elastic model to isolate the steep dip effect. This is done by using elastic finite-difference modeling from a simplified model created to prove the concept that converted wave energy has the potential to increase steep dip subsalt illumination. The elastic model consists of P-wave velocity, S-wave velocity and density attributes required to compute P-wave and  $S_V$ -wave synthetic data which is then migrated using the available conventional acoustic RTM imaging algorithm and a specially designed converted-wave model that considers the constraint of the imaging algorithm.

### 4.1.1 Elastic FDM model building

The simplified elastic model consists of a 1200 m thick water layer, 1800 m thick flat supra-salt sediment layer, 3000 m thick flat salt canopy slab, salt root bounded by a circular arc with dips ranging from 0 to 90° and a flat base of salt at 11000m depth (Figure 33). Each layer contains the average properties of P-wave velocity, S-wave velocity and density derived from the interval velocity model in Figure 13. Each layer is of average thickness in comparison to the more complex modeled in the previous chapter. The  $V_S$  model was computed using the mudrock trend (Castagna, 1993),

$$V_S = 0.86V_P - 1173, \quad (7)$$

where  $V_P$  and  $V_S$  are the P and S-wave velocities in m/s respectively.

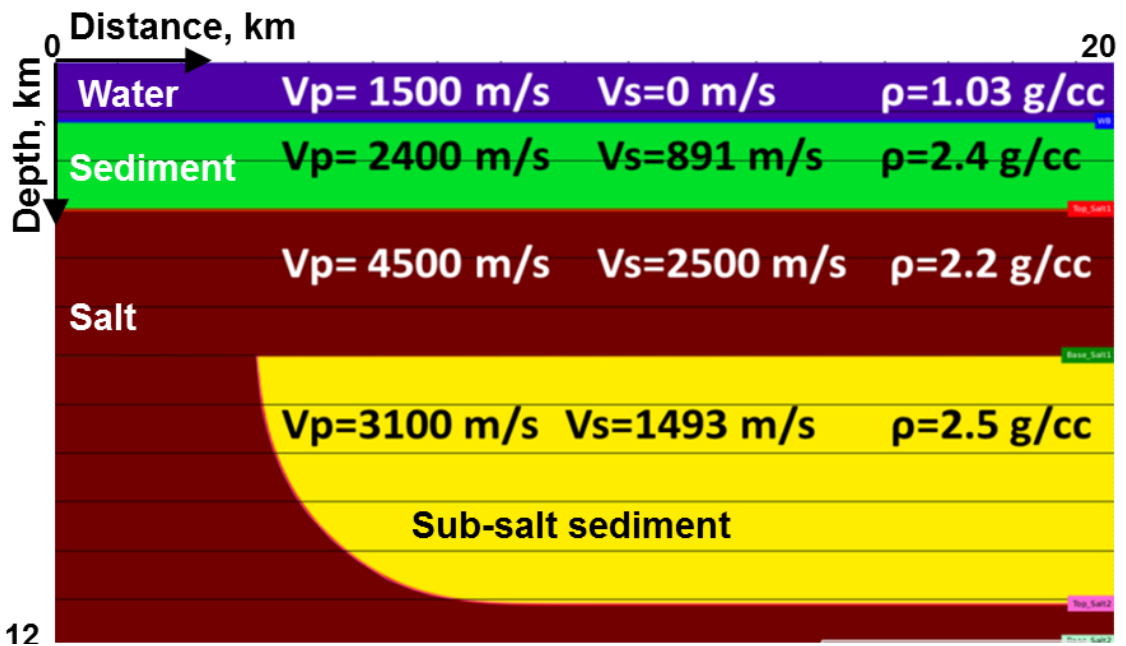


Figure 33 2D elastic FDM model including P-wave velocity, S-wave velocity and density attributes.

In order to determine the contribution of converted waves to the subsalt image under the restriction of an acoustic RTM code that is limited to a single input model, the converted-wave model was built by replacing the P-wave velocity (Figure 34) with its corresponding S-wave velocity in the salt in order to image the converted waves at the salt boundaries (Figure 35). The purpose of this is to correctly image any seismic data that will have a converted wave mode generated at the salt boundary in the elastic synthetic data.

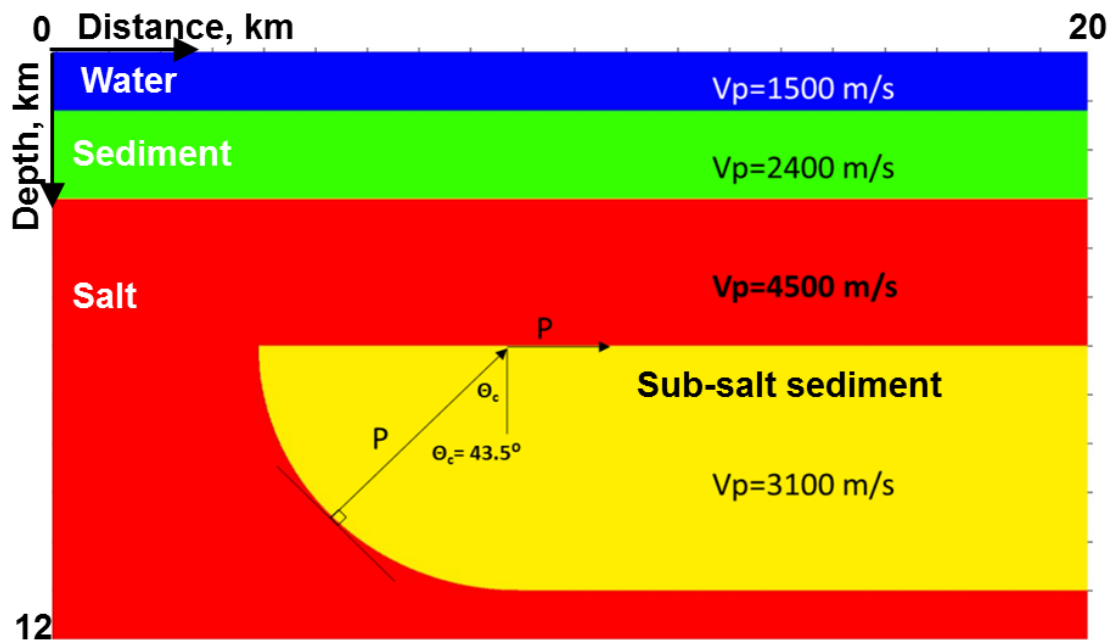


Figure 34 P-wave velocity model used in acoustic RTM to migrate elastic data and a conceptual ray diagram showing the critical reflection of P-wave ray at the base of salt for an up-going incident ray incident at the critical angle.

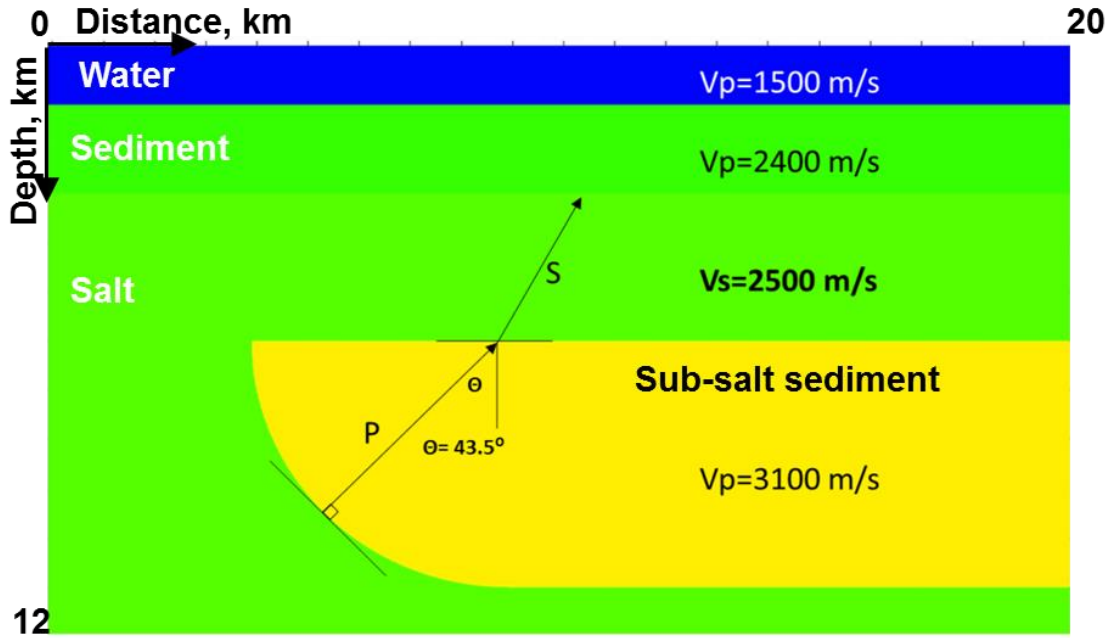


Figure 35 Converted wave model with S-wave salt velocity in the salt layer and a conceptual ray diagram showing the up-going incident P-wave ray and the penetration of the P-S converted ray through the salt.

#### 4.1.2 Elastic forward modeling parameters

An elastic FDM algorithm was used to generate P-wave and converted wave synthetic data from the simplified model shown in Figure 33. Table 6 shows the details of the numerical modeling parameters used in the converted wave modeling.

The source-receiver grid parameters were designed to model the 2D bi-directional acquisition geometry with 8 km cable length in order to generate synthetic data containing S-wave converted energy. Table 7 shows the source-receiver 2D line parameters defined in the elastic finite-difference modeling.

<b>Numerical Model Computation Parameters</b>	
Algorithm	2D Elastic finite-difference
Input datasets	P-wave , S-wave, density models
Grid size	dx = dz = 10 m
Recording length	12 s
Time sample rate	1 ms
Output sample rate	4 ms
Number samples	3001
Source wavelet	Ricker
Dominant frequency	10 Hz

Table 6 Elastic finite-difference modeling computation parameters.

<b>Source-Receiver 2D Line Parameters</b>	
SRD	0 m
Range	0 – 20,000 m
Shot interval	100 m
Number of shots	200
Cable length	8 km
Receiver interval	20 m
Cable layout	Split-spread

Table 7 Source-receiver geometry of split-spread 8 km maximum offset layout.

### 4.1.3 Imaging of synthetic data

The 0-8 km offset synthetic elastic data set was migrated using the acoustic RTM migration algorithm with (1) the P-wave reference FDM velocity model shown in Figure 34 and (2) the converted-wave model shown in Figure 35. The migration parameters used in the migration using both models are shown in Table 8.

<b>RTM migration parameters</b>	
Algorithm	Acoustic RTM
Input datasets	8 km offset synthetic elastic shot gathers
Maximum depth	12000 m
Depth interval	10 m
Migration aperture	14 km
Source wavelet	10 Hz Ricker
Number of shots	200
Shot interval	100 m

Table 8 Acoustic RTM migration parameters for imaging elastic data.

The elastic FDM algorithm computes and outputs the P-wave and  $S_V$ -wave component separately. In imaging, the two datasets are directly used as input into the RTM migration algorithm.

## 4.2 Results

This section describes the results of the elastic finite-difference modeling and subsequent acoustic RTM imaging of the P-wave and converted wave models. For computational efficiency, the FD algorithm outputs the solution to the wave equation shot-by-shot and each shot can be visualized in several ways. The most common ways of representing synthetic shot data generated from wavefield extrapolation methods are via wavefield snapshots and seismograms or common shot gathers.

### 4.2.1 Wavefield snapshots

Wavefield snapshots graphically illustrate the generated elastic synthetic data in the spatial domain at a particular instant in time. Scanning through wavefield snapshots gives the sense of wavefield propagation through the model. Figure 36 (a-f) show wavefield snapshots 0.0, 1.3, 2.1, 2.7, 3.2, and 3.9 seconds, respectively, from a single shot located at with 8 km maximum offset overlaid on the interval layer model. Figure 36 (a) is taken at 0.0s when the wavefield propagation was initiated. Figure 36 (b) is taken at 1.3 s when the reflected P-waves and transmitted P and S-waves can be identified at the water-sediment boundary. Figure 36 (c) shows reflected and transmitted P and S-waves at the interface between sediment and top of salt. Figure 36 (d) shows the reflected and transmitted P and S-waves at the interface between sediment and top of salt as

well as multiples generated from reflections within the supra-salt layer. Figure 36 (e) shows the primary wavefield as it impinges upon the steep dipping salt root. Figure 36 (f) shows the reflected and transmitted P and S-waves at the interface between subsalt sediment and top of the deep salt root. The P and S-wave reflections are down-going but eventually turn as they continue to propagate.

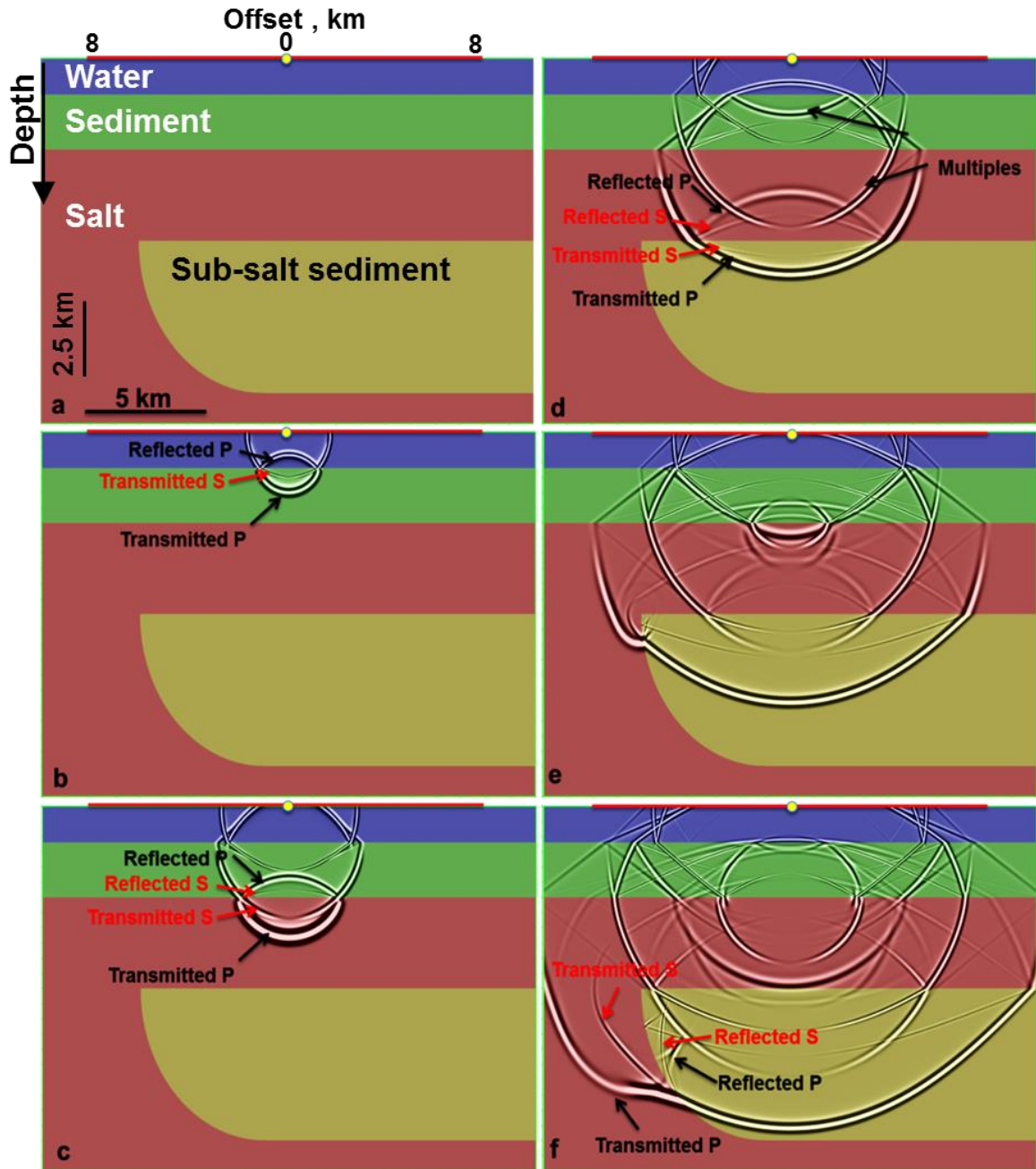


Figure 36 Wavefield snapshots generated from elastic FDM. (a-f) show snapshots at 0.0,1.3, 2.1, 2.7,3.2, and 3.9 seconds respectively from a single shot located at with 8 km maximum offset overlaid on the interval layer model consisting of the water layer (blue) supra-salt sediment layer (green), salt-body (red) and the subsalt sediment layer (yellow).

#### 4.2.2 Elastic synthetic seismogram

The seismogram or shot gather graphically represents the generated synthetic data in terms of source-receiver offset, amplitude and reflection time for a single shot location. Figure 37 shows an example of the seismogram computed using elastic FDM for the same shot location illustrated by the wavefield snapshots in Figure 36 a-f. Each snapshot was taken at the time represented by the dashed line in Figure 37. The seismogram has a record length of 12 s and data with a maximum source-receiver distance of 8 km. The source-receiver split spread geometry for the 8 km maximum offset is represented by the red line at the top of the seismogram. The shot location is shown by the yellow circle.

Displaying the wavefield snapshots as slices in a 3D cube (Figure 38) allows the visualization of the wavefield snapshots in relation to the synthetic seismogram and raypaths at a given offset. This facilitates easy identification of converted wave events and multiples in the synthetic seismogram. Figure 39 (a) shows the relationships among the wavefield snapshot in the left plane, the synthetic seismogram in the top plane and normal incidence/ zero-offset raypaths in the orthogonal plane. Visualization of the normal incidence raypath plane can help to trace the down-going incident ray and identify the primary reflections, multiple reflections and converted wave modes in this simple synthetic case (Figure 39 a and b).

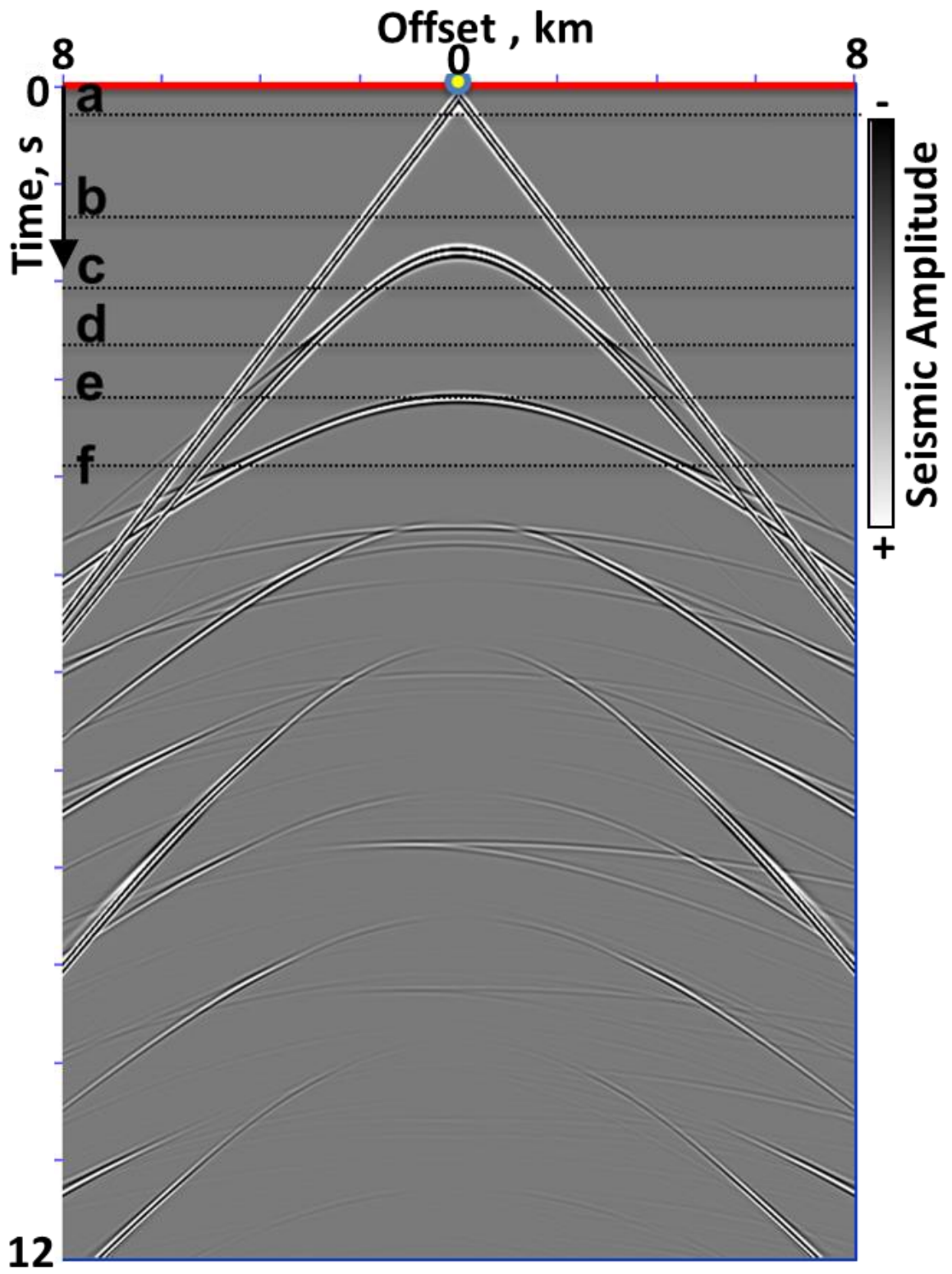


Figure 37 Synthetic seismogram computed using elastic FDM.

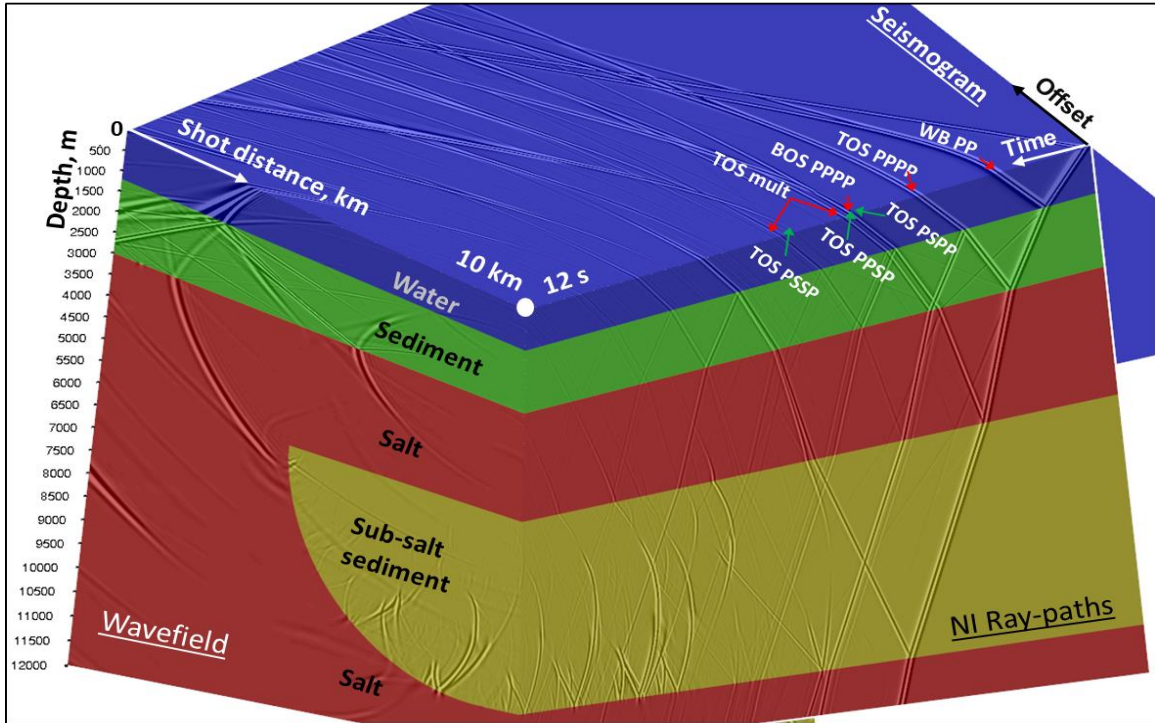


Figure 38 2D Wavefield snapshots stacked in a 3D cube displaying the wavefield, seismogram and normal incidence raypaths in the three orthogonal planes.

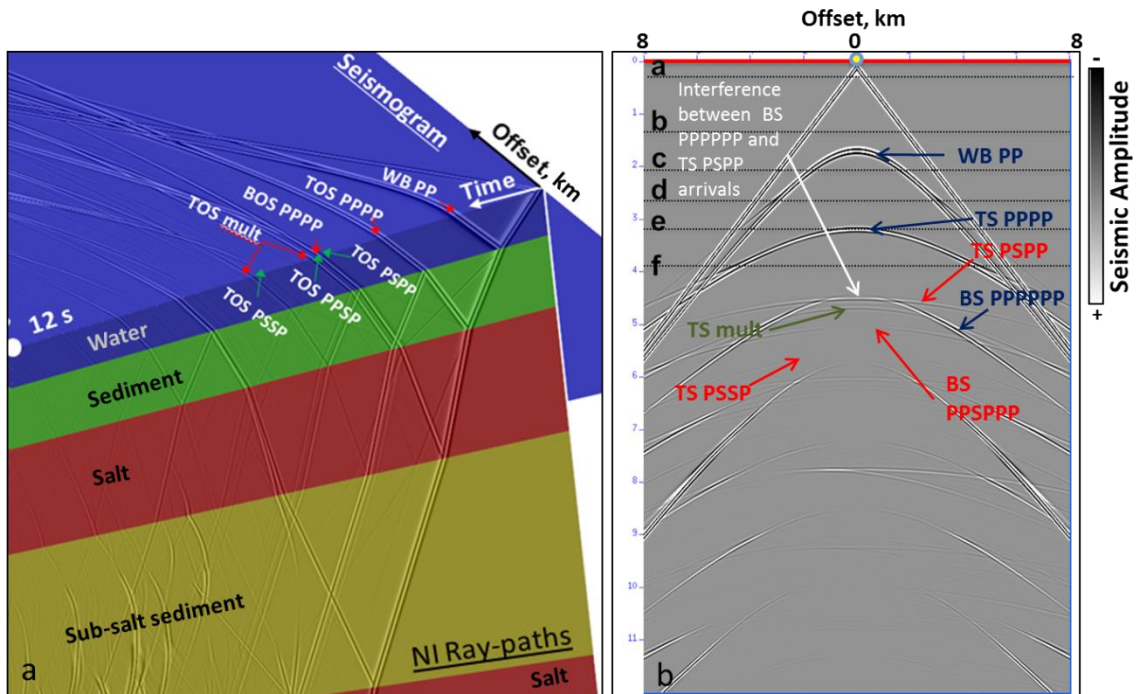


Figure 39 (a) Synthetic data displayed to illustrate the wavefield snapshot, seismogram and normal incidence/ zero-offset raypath and (b) Interpretation of primary, converted wave and multiple events on the seismogram.

### 4.2.3 RTM imaging

Acoustic reverse-time migration was used to image the synthetic data since an elastic RTM was not available. The 2D RTM migration was done using (1) the P-wave model (Figure 34) and (2) the converted wave model with S-wave salt velocity (Figure 35). This was done in an attempt to image the mode conversions at the salt boundary. **Error! Reference source not found.** and **Error! Reference source not found.** show the results of the P-wave RTM and the converted wave RTM respectively. The P-wave imaging condition is not satisfied for the reflection at the deep top of salt and it therefore is not imaged in the converted wave RTM (**Error! Reference source not found.**). In order to illustrate the contribution of the PSP waves to imaging the steep dips, the PSP RTM is superimposed onto the PPP RTM image (Figure 41) and compared.

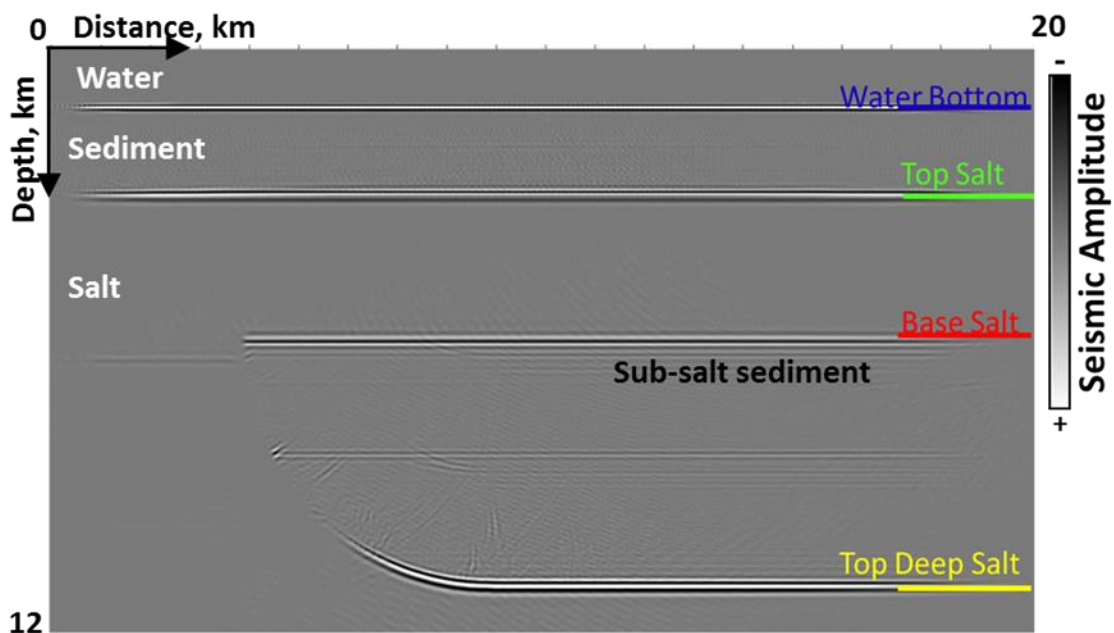


Figure 40 Acoustic RTM of elastic data migrated using the P-wave only velocity model.

The converted wave RTM shows an increase in the range of steep dips imaged. Although the amplitude of the increased dips is low, it must be taken into consideration that only the PSP-PSP mode is properly imaged in **Error! eference source not found..**

The rest of the events contribute to the noise in the migrated stack. This is a limitation of the algorithm chosen to migrate the data. This also shows the likelihood of creating artifacts when different wave modes in the data are unrecognized or mis-identified even with an oversimplified model.

Migration using an elastic RTM algorithm would likely produce a cleaner image and stronger steep dipping events than possible with acoustic RTM by computing the imaging condition for and all of the converted wave modes to their correct positions in depth better focusing the converted wave image.

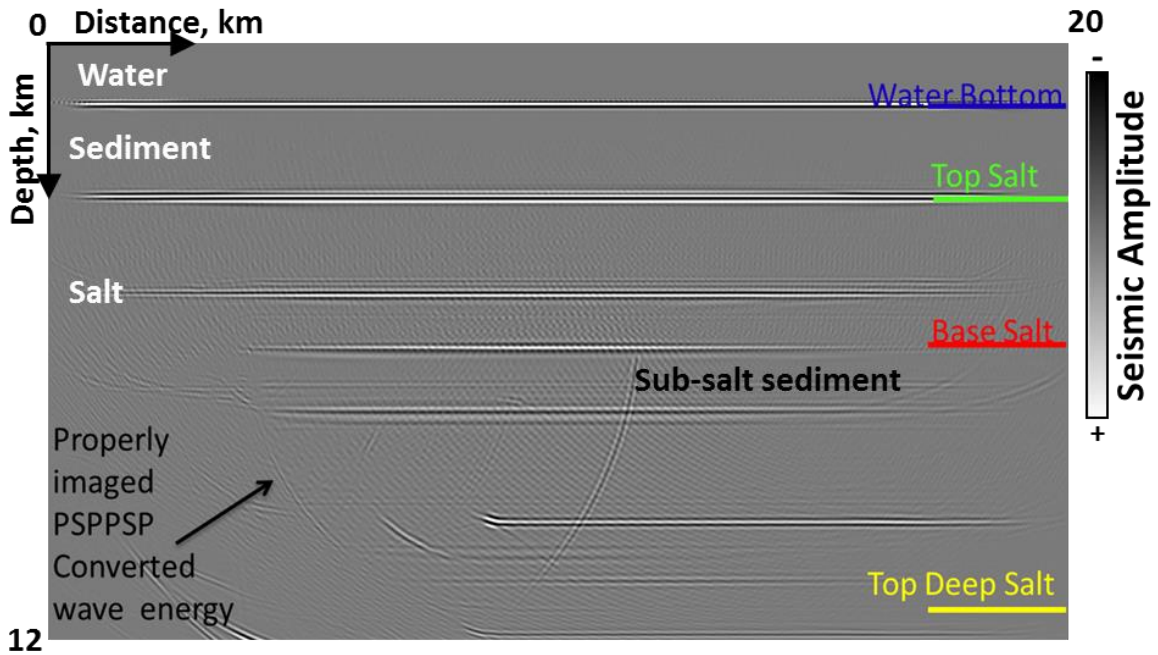


Figure 41 RTM depth migrated section of synthetic elastic data migrated using the converted wave model.

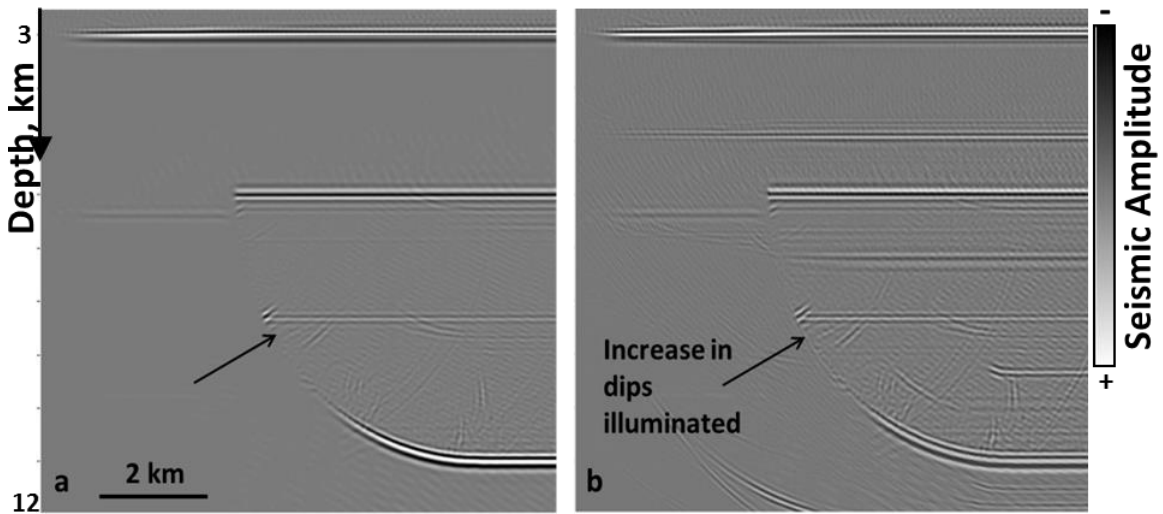


Figure 42 Comparison of (a) P-wave RTM image and (b) the superimposed P-wave RTM and converted wave image.

### 4.3 Discussion

Although the elastic modeling results show that imaging converted waves can increase the dip of illuminated subsalt events, the biggest practical limitation to elastic imaging is the definition of an accurate elastic model. Seismic data acquired from a developed oilfield has the advantage of a good well control beneath the salt. The subsalt velocity elastic model can be much better determined from rock properties of the tested formations and/or shear sonic and density well logs than in areas with limited well control. In order to determine the feasibility of elastic RTM imaging using converted waves in the field, elastic forward modeling should first be used to determine the recording times required for capturing the slow converted waves with the given surface acquisition geometry and a realistic elastic earth model. A sensitivity study is also recommended which should help to determine the effect of error in the P-wave, S-wave and density attributes, as well as geometrical error on the accuracy of the converted wave imaging.

Apart from prismatic wave imaging, imaging with multiples and converted wave imaging, 3D VSP acquisition, processing and modeling have been shown to improve the illumination of steep subsalt dips compared to surface seismic acquisition (Zhuo and Ting, 2011; Hornby *et al.*, 2007). Subsalt steep dips are better imaged by placing receivers below the salt capturing the post-critically reflected energy from the steep dips. Zhuo and Ting (2011) conducted a 3D acoustic FDM study to image steep dips in the Walker Ridge area of the GOM. They modeled NAZ and WAZ surface acquisition and also VSP acquisition

configurations and concluded that surface seismic cannot illuminate subsalt steep dips due to the poor illumination resulting from up-going post-critically reflected off of the base of salt. VSP modeling showed that steep subsalt faults and three-way closures against the salt root were illuminated with subsurface acquisition compared to the surface configurations. Hornby *et al.*, (2007) illustrated that data acquired downhole could be used as a complementary dataset to fill in the illumination holes left by surface acquisition layouts beneath shallow salt.

## 4.4 Conclusions

In this chapter, I used a simple model to prove the concept that migrating converted modes has the potential to improve illumination of steeper dips beneath a high velocity layer with a perfect velocity model. Future work in testing the feasibility of imaging converted waves will evaluate the impact of more realistic model complexity, noise, velocity error using an elastic RTM imaging algorithm. Further modeling can help to determine the optimal recording time and acquisition geometry required to record the different converted wave modes in a realistic model in order to determine the feasibility for imaging different modes from vintage data.

## **Chapter 5 Summary**

The objective of this thesis was to analyze the causes of poor imaging of the events associated with the steeply dipping flanks of a salt feeder in an area of the Gulf of Mexico and to test possible methods of improving the steep dip image by increasing the surface acquisition offset and imaging with converted waves.

In Chapter 2, I first analyzed the illumination of the steeply dipping events beneath the salt canopy in this case study using interactive ray tracing to visualize raypaths from the subsurface target and showed that most of the primary P-wave energy is post-critically reflected at the base of salt and therefore cannot be acquired by surface acquisition. This condition also occurs for gently dipping or flat events reflected off of steeply dipping overlying salt interfaces.

In order to assess the potential for improving the image of the steep subsalt dips, the impact of increasing the maximum acquisition offset was tested by computing ray tracing illumination maps of the subsalt targets for the full azimuth geometry at 8 km and 14 km maximum offsets.

The results showed marginal improvement in illumination of steep dips in the area where the signal to noise ratio is poor. A critical caveat of this method of illumination analysis was that only primary P-wave illumination was modeled and omitted any illumination contribution from wider subsurface angle prismatic waves, mode conversions or multiples.

The method of full-wavefield modeling and imaging has the advantage that it naturally handles prismatic waves and multi-pathing better than the ray tracing method. Using finite-difference modeling, I was able to obtain better illumination results and conclusions about the contribution of longer offsets.

I used acoustic variable density finite-difference modeling and RTM imaging of a 2D model to generate synthetic data with maximum offsets of 8 km and 14 km, and RTM migrated the datasets with the perfect model to compare the impact of the increased offset.

The results of Chapter 3 suggested that increasing data acquisition maximum offset from 8 km to 14 km can contribute to the acoustic illumination of steeply dipping targets by imaging prismatic waves captured by the 14 km maximum offset geometry and also through undershooting the edge of the salt canopy. The geometry of the top of deep salt plays a critical role in focusing prismatic waves toward the steep dip 'attic' region of the feeder.

These conclusions are valid not only for this case study, but also for all of the Gulf of Mexico, however, since the minimum offset required in order to capture prismatic waves will vary largely depending on the geometry of the salt canopy and the geometry of the sub-canopy reflective boundary, full-wavefield seismic forward modeling is critical to optimizing the workflow for future improvement of the data. In this case, ray tracing modeling of prismatic waves and very-long offset undershooting geometries can help in the determination of the minimum offset and

acquisition time required in order to capture this energy at the surface with careful parameterization of the ray tracing to include high angle prismatic waves.

The results of Chapter 4 proved that converted waves can potentially improve the illumination of subsalt steep dips. Since the S-wave velocity of salt is slower than the P-wave velocity of its surrounding sediment, P-S converted waves up-going from the base of salt do not suffer from the critical angle limitation of P-waves. A simple model was used in testing the impact of converted wave illumination compared to P-wave illumination on a boundary ranging in dips from 0 to 90°. Although the acoustic RTM imaging method used in this study was only able to image one of the various modes converted at the base of salt, the results confirm that steeper dips can be illuminated using converted waves than with P-wave imaging only. Full elastic RTM can provide more conclusive evidence to support these findings by satisfying the imaging condition for all of the converted wave modes, however improving the image in the field will require very accurate definition of the P-wave velocity, S-wave velocity and density model.

In addition to prismatic waves and converted waves, imaging with multiples similar to that done by Liu *et al.*, (2011) can also enhance the illumination of steep subsalt dips due to the large variety of raypaths traveled by the multiples and the smaller angle range of multiply reflected waves. Imaging with multiples rather than eliminating multiples could allow more information of the subsurface to be

extracted from the vintage data by correct positioning of reflection events using the correct model.

VSP acquisition can also greatly enhance the imaging of steep subsalt dips by capturing the high energy post-critically reflected P-wave energy off of the base of salt canopy. However, VSP acquisition may be economically infeasible given the relatively high cost of the acquisition method compared to surface acquisition; therefore it is recommended to continue to investigate alternative methods of improving the image of existing data already acquired at the surface.

This modeling study confirms the benefit of acquiring longer offset data imaging using prismatic waves; and the benefit of imaging converted waves in order to improve steep dip subsalt imaging with surface data acquisition, given a sufficiently accurate velocity model.

Although the effective improvement of the image using prismatic and converted waves shown in this case were individually small, the combined benefits of increased offset, migrating with multiples and using converted waves may further improve low-illumination steep dip image with an accurate model. The acquisition of prismatic waves and converted waves can benefit from the longer offset data and also extra-long recording times. A separate modeling experiment can be done to determine the required recording times for these non-primary wave types. Future work is recommended to examine the impact of imaging with multiples and downhole seismic data in this field.

All of the methods of imaging multiply reflected energy are highly model-dependent. This is a significant practical limitation in complex areas where an accurate velocity model is difficult to define. In addition to improving imaging algorithms that image of non-primary P-wave energy such as prismatic waves and converted waves, continuous improvement in accurately defining the earth model will help to improve imaging the illumination holes in current images by making these advanced imaging methods more feasible.

## References

- Aki, K., and P.G. Richards, 1980, Quantitative Seismology: Theory and methods, vol. 1: W.H. Freeman & Co.
- Baysal, E., D. D. Kosloff, and W. C. J. Sherwood, 1983, Reverse time migration: Geophysics, **48**, 1514–1524.
- Bednar, J., 2005, A brief History of seismic migration time: Geophysics, **70**, 3MJ–20MJ.
- Biondi, B. and G. Shan, 2002, Pre-stack imaging of overturned reflections by reverse time migration: SEG Technical Program Expanded Abstracts, **21**, 1284–1287.
- Brittan, J., J. Bai, H. Delome, C. Wang and D. Yingst, 2013, Full waveform inversion – the state of the art, First Break, **31**, 75-78
- Carcione, J., G. Herman, and T. Kroode, 2002, Seismic Modeling: Geophysics, **67**, no. 4, 1304–1325.
- Castagna, J., 1993, Petrophysical imaging using AVO: The Leading Edge, **12**, no. 3, 172-178.
- Červený, V., 2001, Seismic Ray Theory: Cambridge University Press.
- Claerbout, J., 1971, Towards a unified theory of reflector mapping: Geophysics: **36**, 467–481.
- Cogan, M., J. Gardner and N. Moldoveanu, 2011, A deep-water Gulf of Mexico subsalt imaging analysis with finite-difference modeling: 81st SEG Congress and Exhibition 2011, Extended Abstracts, 3233–3237.
- Diaz, E. and P. Sava, 2012, Understanding the reverse time migration backscattering: Noise or signal?: 2012 SEG Annual Meeting, 4–9 November, Las Vegas, Nevada.
- Farmer, P., I. Jones, H. Zhou, R. Bloor and M. Goodwin, 2006, Application of reverse-time migration to complex imaging problems: First Break, **24**, no. 9, 65–73.

- Fletcher, R., P. Fowler, P. Kitchenside, and U. Albertin, 2005, Suppressing artifacts in pre-stack reverse-time migration: 75th Annual International Meeting, SEG, Expanded Abstracts, 2049–2051.
- Gardner, G., Gardner L., Gregory A., 1974, Formation velocity and density - the diagnostic basics for stratigraphic traps: *Geophysics* **39**, 770–780.
- Gjøystdal, H., E. Iversen, R. Laurain, I. Lecomte, V. Vinje, and K. Åstebøl, 2002, Review of ray theory applications in modeling and imaging of seismic data: *Studia Geophysica et Geodaetica*, **46**, no. 2, 113–164.
- Gray, S., J. Etgen, J. Dellinger, and D. Whitmore, 2001, Seismic migration problems and solutions: *Geophysics*, **66**, 1622–1640.
- Hornby, B., J. Sharp, J. Farrelly, S. Hall, and H. Sugianto, 2007, 3D VSP in the deep water Gulf of Mexico fills in subsalt 'shadow zone': *First Break*, **25**, 83–88.
- Kaelin B., and A. Guitton, 2006, Imaging condition for reverse time migration: Expanded Abstracts, 76th SEG Annual International Meeting, Society of Exploration Geophysicists, 2594–2598.
- Li, H., J. Kapoor, N. Moldoveanu, B. Dragoset and K. Jiao, 2010, Evaluation of longer offsets to subsalt imaging through elastic modeling: 80th Annual International Meeting, SEG, Expanded Abstracts, 3008–3012.
- Li, Y., Q. Wu, M. Wang and T. Huang, 2014, Benefits of full-azimuth and ultra long-offset data for subsalt imaging in the deepwater Gulf of Mexico: *The Leading Edge*, **33**, no. 9, 996–998.
- Liao Q., D. Ramos, W. Cai, S. Muskaj, F. Ortigosa, 2009, Subsalt illumination analysis through ray tracing and seismic modeling: a GOM case study; Extended Abstracts, 71st EAGE Congress and Exhibition 2009.
- Lines, L., R. Slawinski, and R. Bording, 1999, A recipe for stability analysis of finite-difference wave equation computations: *Geophysics*, June 1999, **64**, 967–969.
- Liu, Y., X. Chang, D. Jin, R. He, H. Sun, and Y. Zheng, 2011 Reverse time migration of multiples for subsalt imaging: *Geophysics*, **76**, no. 5, WB 201–216.
- Mandroux, F., B. Ong, C. Ting, S. Mothi, T. Huang and Y. Li, 2013, Broadband, long-offset, full azimuth, staggered marine acquisition in the Gulf of Mexico: *The Leading Edge*, **31**, 125–132.

- Marfurt, K., 1984, Accuracy of the finite-difference and finite-element modeling of the scalar and elastic wave equations: *Geophysics*, **49**, 533–549.
- Moczo, P., O. Robertsson and L. Eisner, 2007, The Finite-Difference Time-Domain Method for Modeling of Seismic Wave Propagation: *Advances in Geophysics*, **48**, pp. 421–516.
- Muerdter, D. and D. Ratcliff, 2001, Understanding subsalt illumination through ray trace modeling, Part 2: Dipping salt bodies, salt peaks, and nonreciprocity of subsalt amplitude response: *The Leading Edge*, **20**, no. 8, 803–816.
- Muerdter, D., R. Lindsay and D. Ratcliff, 1996, Imaging under the edges of salt sheets: a ray tracing study: 66th SEG Conference and Exhibition, SEG Technical Program Expanded Abstracts 1996, 578–580.
- Ogilvie, J., and G. Purnell, 1996, Effects of salt related mode conversions on subsalt prospecting: *Geophysics*, **61**(2), 331–348.
- Purnell, G., 1992, Imaging beneath a high-velocity layer using converted waves: *Geophysics*, **57**, 1444–1452.
- Schneider, W., and G. Winbow, 1999, Efficient and accurate modeling of 3-D seismic illumination: 69th Annual International Meeting, Expanded Abstracts, 633–636.
- Tang, Y., 2008, Wave-equation hessian by phase encoding: 78th Annual International Meeting, SEG, Expanded Abstracts, 2201–2205.
- Verschuur, D., and A. Berkhout, 2005, Transforming multiples into primaries: experience with field data: 75th Annual International Meeting, SEG, Expanded Abstracts, 2103–2106.
- Wu, R.S., R. Yan, X. B. Xie, and D. Walraven, 2010, Elastic converted-wave path migration for subsalt imaging: SEG Technical Program Expanded Abstracts, 3176–3180.
- Yoon, K., and K. Marfurt, 2006, Reverse-time migration using the pointing vector: *Exploration Geophysics*, **37**, 102–107.
- Youn, O. K., and H. Zhou, 2001 Depth imaging with multiples: *Geophysics*, **66**, 246–255.

Zhang, Y., and J. Sun, 2009, Practical issues in reverse time migration: true amplitude gathers, noise removal and harmonic source encoding: First Break, **26**, pp. 29–35.

Zhuo L., and C. Ting, 2011, Subsalt steep dip imaging study with 3D acoustic modeling: 73rd EAGE Conference and Exhibition, Extended Abstracts, 23–26.